

Deciphering interventional dynamical causality from non-intervention systems

Jifan Shi^{1,2,3}, Yang Li⁴, Juan Zhao⁵, Siyang Leng^{1,6}, Kazuyuki Aihara^{4*},
Luonan Chen^{4,7,8*}, Wei Lin^{1,2,3*}

¹Research Institute of Intelligent Complex Systems, Fudan University, Shanghai 200433, China

²Shanghai Artificial Intelligence Laboratory, Shanghai 200232, China

³State Key Laboratory of Medical Neurobiology and MOE Frontiers Center for Brain Science, Fudan University, Shanghai 200032, China

⁴International Research Center for Neurointelligence, The University of Tokyo Institutes for Advanced Study, The University of Tokyo, Tokyo 113-0033, Japan

⁵School of Pharmacy, Shanghai University of Traditional Chinese Medicine, Shanghai 201203, China

⁶Academy for Engineering and Technology, Fudan University, Shanghai 200433, China

⁷Key Laboratory of Systems Biology, Shanghai Institute of Biochemistry and Cell Biology, Center for Excellence in Molecular Cell Science, Chinese Academy of Sciences, Shanghai 200031, China

⁸Key Laboratory of Systems Health Science of Zhejiang Province, School of Life Science, Hangzhou Institute for Advanced Study, University of Chinese Academy of Sciences, Chinese Academy of Sciences, Hangzhou 310024, China

*To whom correspondence should be addressed; E-mail: kaihara@g.ecc.u-tokyo.ac.jp or lnchen@sibs.ac.cn or wlin@fudan.edu.cn.

Detecting and quantifying causality is a focal topic in the fields of science, engineering, and interdisciplinary studies. However, causal studies on non-intervention systems attract much attention but remain extremely challenging. To address this challenge, we propose a framework named Interventional Dynamical Causality (IntDC) for such non-intervention systems, along with its computational criterion, Interventional Embedding Entropy (IEE), to quan-

tify causality. The IEE criterion theoretically and numerically enables the deciphering of IntDC solely from observational (non-interventional) time-series data, without requiring any knowledge of dynamical models or real interventions in the considered system. Demonstrations of performance showed the accuracy and robustness of IEE on benchmark simulated systems as well as real-world systems, including the neural connectomes of *C. elegans*, COVID-19 transmission networks in Japan, and regulatory networks surrounding key circadian genes.

Introduction

Directional or indirectional interactions among different components give rise to a variety of complex phenomena in nature and social society. The causality or the causal effect is one of the most attractive directional relations originating from the non-reversibility of time. Modeling, detecting, and quantifying causality from observational data are crucial for describing, interpreting, predicting, and even controlling complex systems.

Statisticians believe that the causality is contained and obtainable in universal random variables regardless of the time label. The Neyman-Rubin's potential outcome framework (1–3), the Wright's structural equation model (4, 5) and the Pearl's causal diagram model (6, 7) are the most famous statistical approaches, which have been proved to be of mathematical equivalence (8). Especially, the instrumental variable method, that was awarded the 2021 Nobel Prize in economic sciences, is widely applied in the study of causality among economics, environments, and other disciplines (9). Statistical methods seek to discern binary causal relations among random variables on a directed acyclic graph, without relying on temporal data. However, in general complex dynamical systems, the causation must precede the effect, feedback is common, and the causal strength needs to be quantitatively measured. Time should play

definitely a key role.

Dynamics-oriented researchers have proposed fruitful algorithms for measuring the observational causality from time series, commonly referred to as the dynamical causality (10). The celebrated Granger causality (GC) (11, 12) employs a linear model and uses improvement of predictability over time to illustrate the causality. Transfer entropy (TE) (13) generalizes GC to the nonlinear case by quantifying the prediction uncertainty through Shannon entropy. Neither GC nor TE addresses the “non-separability” problem, which means that removing the causal variable from the system inevitably influences the dynamics of downstream variables (10, 14–16). To measure causality in non-separable systems, numerous approaches have emerged in the last decade within the framework of delay embedding. These include convergence of cross mapping (CCM) (14, 17), partial cross mapping (PCM) (15), continuity scaling (16), inverse continuity (18), topological expansion (19), joint distance distribution (20), embedding entropy (EE) (10) and other indices (21, 22).

Nonetheless, most indices designed for quantifying the dynamical causality primarily estimate directional causal relations at the observational level, i.e. observational dynamical causality (ObsDC). Conventionally, to detect and quantify causality at the interventional level, which is noted as the interventional dynamical causality (IntDC) in this study, intelligent modulation and manipulation of the dynamical system should be taken into account. By allowing external intervention to the system and recording data under different perturbations, frameworks such as perturbation cascade inference (PCI) (23) and dynamical causal effect (DCE) (24, 25) provide relevant computational schemes. However, due to ethical or practical limitations, many real systems should be analyzed without any external intervention. An essential problem is how to measure IntDC solely from the observational data but at the interventional level.

In this study, we propose the IntDC framework and introduce a criterion named Interventional Embedding Entropy (IEE), which aims to identify and quantify IntDC between variables

solely from the observational time series. Actually, IEE is rigorously derived by the theory of the delay embedding. Numerical IEE does not require specific prior knowledge of dynamics, and additional perturbation to the system is also unnecessary. Compared to ObsDC indices, IEE designed for IntDC has the capability to rank the importance of causal effects and construct directional causal networks more effectively. We demonstrate numerical experiments on both simulated examples and real datasets, including estimating neural connectomes of *C. elegans*, evaluating COVID-19 transmission in Japan, and constructing regulatory networks surrounding key circadian genes.

Methods

Observational dynamical causality in delay-embedding space

We consider a discrete two-variable dynamical system as

$$\begin{cases} x_{t+1} = g(x_t, x_{t-1}, \dots, x_{t-p}, \varepsilon_{x,t}), \\ y_{t+1} = f(x_t, x_{t-1}, \dots, x_{t-p}, y_t, y_{t-1}, \dots, y_{t-p}, \varepsilon_{y,t}), \end{cases} \quad (1)$$

where x, y are two variables, p denotes the time step during which causality is considered, and $\varepsilon_{\cdot,t}$ stand for small noise terms. According to *Shi et al. (10)*, there exists ObsDC from x to y since the evolving equation of y_{t+1} depends on the historical behavior of x , while there is no ObsDC from y to x as the dynamics of x_{t+1} is independent of y . GC and TE measure the predictability of f in the original time-series space to quantify the ObsDC from x to y through linear regression and entropy uncertainty, respectively (Fig. 1(B)). The causal strength of GC/TE is based on the assumption of separability, which means that removing x from the system does not influence the observed data of y . However, in general coupled systems, the separability is not satisfied, as removing one variable changes the values of affected ones (14–16).

To address the challenge of detecting ObsDC in universal non-separable systems, various

approaches from the delay-embedding space have been proposed. In the delay-embedding framework, the bivariate system Eq. (1) is assumed to evolve into an attractive manifold with an inner dimension d . Let the time-delay vectors of x and y be

$$\mathbf{X}_t = (x_t, x_{t-1}, \dots, x_{t-L})^T \in \mathcal{M}_X \subseteq \mathbb{R}^{L+1}, \quad (2)$$

and

$$\mathbf{Y}_{t+1} = (y_{t+1}, y_t, y_{t-1}, \dots, y_{t-L+1})^T \in \mathcal{M}_Y \subseteq \mathbb{R}^{L+1}, \quad (3)$$

where L is the time-delay length, \mathcal{M}_X and \mathcal{M}_Y represent the manifolds formed by \mathbf{X}_t and \mathbf{Y}_t , respectively. According to the seminal stochastic version of Takens' embedding theorem (26–29), for delay dimension $L \geq 2d$, we can obtain

$$\mathbf{X}_t = \mathbf{F}(\mathbf{Y}_{t+1}), \quad (4)$$

where \mathbf{F} is a smooth projection operator. The detailed derivation can be referred to the Supplementary Text. Equation (4) shows that the causal variable $\mathbf{X}_t \in \mathcal{M}_X$ can be reconstructed by the effect variable $\mathbf{Y}_{t+1} \in \mathcal{M}_Y$. However, as \mathbf{F} is not reversible in generic sense, we can not determine \mathbf{Y}_{t+1} only by the information from \mathbf{X}_t . The causal dependence in f between x and y is transformed into the reconstructability of \mathbf{F} (Fig. 1(D)). Instead of fitting a model by removing the causal variable as in GC and TE, detecting the existence and quantifying the continuity characteristics of \mathbf{F} in the delay-embedding space can be adequate for causal identification, especially for universal non-separable systems. Related algorithms include CCM, PCM, and EE.

Figures 1(A), (B) and (D) summarize dynamical causality at the observational level, where the ObsDC from variable x to y is estimated only from the historical observed time series. But fitting Eq. (1) or Eq. (4) from data is criticized as mere association or prediction (30, 31).

Interventional dynamical causality in delay-embedding space

The detection of hidden essential-level causality necessitates intervention or manipulation to the system (8, 23, 32, 33). We define that there is an IntDC from x to y during the time $[t-p, t]$ in the original time-series space, if $\delta y_t = \tilde{y}_t - y_t$ depends on $\delta x_t = \tilde{x}_t - x_t$, where the dynamics of x_t is perturbed to \tilde{x}_t , and \tilde{y}_t is the dynamics of affected y after the perturbation (Fig. 1(C)). The intervention δx_t can be either a pulse stimulation or persistent disturbances to the system.

To measure the IntDC, data before and after the intervention, i.e. (x_t, y_t) and $(\tilde{x}_t, \tilde{y}_t)$, are typically required, as in PCI and DCE. These conventional algorithms rely on reproducible dynamics or data availability under different settings.

To address challenges of causal inference in widespread non-intervention, non-linear and non-separable systems, we turn to the study of intervened dynamics Eq. (4) in the delay-embedding space. Denote $\delta \mathbf{X}_t = \widetilde{\mathbf{X}}_t - \mathbf{X}_t$ and $\delta \mathbf{Y}_{t+1} = \widetilde{\mathbf{Y}}_{t+1} - \mathbf{Y}_{t+1}$, where $\widetilde{\mathbf{X}}_t$ and $\widetilde{\mathbf{Y}}_{t+1}$ are the time-delay vectors of x and y after the intervention, respectively. Under infinitesimal intervention, Eq. (4) leads to

$$\delta \mathbf{X}_t = \nabla_{\mathbf{Y}} \mathbf{F}(\mathbf{Y}_{t+1}) \cdot \delta \mathbf{Y}_{t+1}. \quad (5)$$

Equation (5) indicates that $\delta \mathbf{Y}_{t+1}$ contains complete information of $\delta \mathbf{X}_t$ in the neighborhood of \mathbf{Y}_{t+1} or reconstructs $\delta \mathbf{X}_t$, if there exists IntDC from the causal variable x to the effect variable y (Fig. 1(E)).

Figures 1(A), (C), and (E) give an overview of the IntDC framework.

Interventional embedding entropy

We introduce the IEE criterion, specifically designed for quantifying IntDC solely from the observational data in the delay-embedding space. The IEE criterion is proposed to measure the average information retention or reconstructability from the effect $\delta \mathbf{Y}_{t+1}$ to the causation $\delta \mathbf{X}_t$,

formulated as

$$\text{IEE}[x \rightarrow y] = \text{CMI}(\delta \mathbf{X}_t, \delta \mathbf{Y}_{t+1} | \mathbf{Y}_{t+1}), \quad (6)$$

where CMI is the conditional mutual information (34), i.e.

$$\text{CMI}(\mathbf{x}, \mathbf{y} | \mathbf{z}) = \iiint p(\mathbf{x}, \mathbf{y}, \mathbf{z}) \log \frac{p(\mathbf{x}, \mathbf{y} | \mathbf{z})}{p(\mathbf{x} | \mathbf{z}) p(\mathbf{y} | \mathbf{z})} d\mathbf{x} d\mathbf{y} d\mathbf{z}. \quad (7)$$

The $\delta \mathbf{Y}_{t+1}$ is estimated by the distance from \mathbf{Y}_{t+1} to its neighbored points \mathbf{Y}_{t_k+1} in the embedding space, and $\delta \mathbf{X}_t$ is calculated by \mathbf{X}_{t_k} with the same time label t_k (Figs. 1(E) and (F)). Thus, Eq. (6) can be numerically approximated only from the observational data, especially for non-intervention systems. Table 1 shows the numerical algorithm for IEE, whose detailed derivation can be found in the Supplementary Text.

Results

IEE can accurately and robustly quantify causality

To assess the numerical performance of measuring IntDC, we first applied the IEE algorithm on the following two-node Logistic dynamics

$$\begin{cases} x_{t+1} = 3.7[(1 - \beta_{yx})x_t(1 - x_t) + \beta_{yx}y_t(1 - y_t)] + \varepsilon_{x,t}, \\ y_{t+1} = 3.7y_t[1 - (1 - \beta_{xy})y_t - \beta_{xy}x_t] + \varepsilon_{y,t}, \end{cases} \quad (8)$$

where $\varepsilon_{.,t}$ represents independent Gaussian noises, and parameters β_{xy} and β_{yx} modulate the IntDC strength from x to y and from y to x , respectively (see further details in SM).

IEE can accurately capture the numerical behavior of dynamical causality in the two-node Logistic system, especially IntDC rather than ObsDC. In Fig. 2(A), we set $\beta_{xy} \equiv 0$ and let β_{yx} increase from 0 to 0.3. We observed a monotonic increase in $\text{IEE}[y \rightarrow x]$ (the red line with squares), while $\text{IEE}[x \rightarrow y]$ remained around zero (the blue line with dots). In Fig. 2(B), we set $\beta_{xy} \equiv 0.1$ and let β_{yx} increase from 0 to 0.3. $\text{IEE}[y \rightarrow x]$ exhibited a monotonic increase (the red line with squares), while $\text{IEE}[x \rightarrow y]$ stayed above zero (the blue line with dots). The

gray dashed lines in Figs. 2(A-B) represent 0.01 for reference. A detailed comparison with GC, TE and CCM can be found in figs. S1 and S2, which indicate that GC exhibited non-monotonic behavior, $TE[y \rightarrow x]$ slightly decreased with a false-negative issue, and $CCM[x \rightarrow y]$ had a false-positive problem. The mean values and standard deviations of the indices under 100 simulations are provided in tables S1-S4.

Within suitable parameter ranges, IEE demonstrates stability and robustness. In Figs. 2(D-G), we validated the robustness of the IEE algorithm under various conditions, including different delayed lags L , the numbers of nearest neighbors K , lengths of time series N , and noise amplitudes σ . The causal strength should exhibit a descending trend with decreasing β_{yx} from 0.15 to 0.05 through 0.125, 0.1, 0.075. The experiments support that IEE maintains the correct order under different parameter values with relatively stable variations.

IEE can eliminate the effects of confounding variables

IEE remains applicable and accurate even in presence of confounding variables. We simulated a three-node Logistic dynamics (x_t, y_t, z_t) , where z acted as a confounder (see details in SM). There were consistently non-zero causal effects from z to x and from z to y , while β_{xy} adjusted the causal strength from x to y (Fig. 2(C)). When $\beta_{xy} = 0$, $IEE[x \rightarrow y]$ was almost zero and significantly different from $IEE[z \rightarrow x]$ and $IEE[z \rightarrow y]$ (Fig. 2(C)); but conventional ObsDC indices such as GC/TE/CCM produced false-positive causality from x to y due to the presence of confounder z (fig. S3). That is because an intervention on x , i.e. δx , will not induce δy through z under the IntDC framework. IEE, specially designed for measuring IntDC, remained unaffected by the confounder z and yielded accurate results.

IEE can reconstruct causal networks with quantified causal strength

IEE has the capability to reconstruct the causal network structure and rank the causal influence between nodes in complex networks at the interventional level. We used a 10-node coupled Henon maps as an example, where each node serves as the dynamical cause to its subsequent node (Fig. 3(A)). Further details regarding the dynamics can be found in SM.

To verify the effectiveness of IEE in reconstructing causal networks, we calculated the Area Under Curve (AUC) values based on multiple simulated time series. The AUC value of IEE was 0.871 ± 0.008 , significantly higher than conventional ObsDC indices, such as GC with 0.707 ± 0.069 , TE with 0.816 ± 0.018 , and CCM with 0.837 ± 0.012 . The boxplots for AUC values are displayed in Fig. 3(B). AUCs for IEE exhibited a higher mean and a smaller variation compared to the others. Additionally, fig. S4 presents receiver operating characteristic (ROC) curves.

To show the capability for ranking the importance of causal influences, we conducted two tests. We first calculated the IEE from Node 1 to the other nine nodes. Consistently with the actual scenario, IEE displayed sequential decrease in IntDC originating from Node 1 across Nodes 2 to 10 (Fig. 3(C)). Then, we measured the IEE received by Node 7 from the other nine nodes. As expected, Nodes 1-6 exhibited ascending causal strengths on Node 7, whereas Nodes 8-10 had little influence on Node 7 (Fig. 3(D)). IEE accurately discerned the IntDCs, with Node 6 showing the strongest value. A comparison between IEE for the IntDC and the results from GC, TE, and CCM for the ObsDC can be found in figs. S5 and S6. GC and TE failed to rank the influence from Node 1 accurately (fig. S5), while CCM suffered from the false-positive causal detection from Node 8 to Node 7 (fig. S6).

IEE can quantify IntDC effectively without requiring interventions or perturbations

IEE is specifically designed for calculating IntDC solely from observed time-series data without requiring additional perturbations to the system. To validate its accuracy, we conducted a comparison against true perturbed deviations using chaotic neural networks (chNNs) as a model system (35, 36).

The chNN comprises an output variable $\mathbf{x} = (x_1, x_2, \dots, x_{N_{\text{node}}})^T$ and two internal variables, with N_{node} representing the number of neurons in the network. We chose $N_{\text{node}} = 10$ in simulations. Details on the dynamics can be found in SM. We denoted the observed time-series data from the stationary system without intervention as \mathbf{x}_{obs} . When the neuron i was removed (set as a constant zero), the perturbed data were denoted as $\mathbf{x}_{\text{per}}^{(i)}$. Removing one node was taken as an intervention to the system. The stationary probability density functions of the j th neuron before and after the intervention were represented by $p_j(\mathbf{x}_{\text{obs}})$ and $p_j(\mathbf{x}_{\text{per}}^{(i)})$, respectively. We used the Kullback-Leibler divergence (KLD), i.e.

$$\begin{aligned} D_{ij} &\triangleq \text{KLD}[p_j(\mathbf{x}_{\text{obs}}) || p_j(\mathbf{x}_{\text{per}}^{(i)})] \\ &= \iint p_j(\mathbf{x}_{\text{obs}}) \log \frac{p_j(\mathbf{x}_{\text{obs}})}{p_j(\mathbf{x}_{\text{per}}^{(i)})} d\mathbf{x}_{\text{obs}} d\mathbf{x}_{\text{per}}^{(i)}, \end{aligned} \quad (9)$$

to quantify the true influence of the intervention, i.e. IntDC, from i to j . By conducting 100 randomly simulated chNNs with interventions (10 removed nodes for each chNN), we recorded 1000 KLD values and compared them with the results of IEE (calculated from \mathbf{x}_{obs} solely). In Fig. 4(A), gray dots are the 1000 samples of causal edges between neurons, while the red line stands for the linear regression. We observed that $\text{IEE}[x_i \rightarrow x_j]$ exhibited a positive linear correlation with the KLD D_{ij} (with $R^2 = 0.869$). Results for GC (with $R^2 = 0.572$), TE (with $R^2 = 0.912$), and CCM (with $R^2 = 0.622$) are shown in Figs. 4(B-D), which imply that GC and CCM cannot linearly reflect KLD. Furthermore, the violin plots of cosine similarity S_c

(see SM) between KLD and the four causal indices on 100 chNNs are displayed in Fig. 4(E). IEE (0.904 ± 0.024) had the highest mean similarity with KLD, compared to GC (0.711 ± 0.076), TE (0.888 ± 0.022), and CCM (0.687 ± 0.033). These results indicate that IEE can accurately quantify IntDC from \mathbf{x}_{obs} alone, alleviating the need for additional interventions to the dynamics.

Application of IEE in inferring neural connectomes of *C. elegans*

We applied the IEE criterion to infer the neural connectomes of *Caenorhabditis elegans* (*C. elegans*), a model organism known for its comprehensively studied nervous system (37). Calcium fluorescence imaging time series data from 31 neurons with specific functions of a freely moving *C. elegans* were collected from Kato *et al.* (38) (see Figs. 5(A-B) and fig. S7). The Fig. 5(C) shows the cosine similarity matrix between different neurons. We clustered the neurons into 7 clusters after data preprocessing (see details in Supplementary Text and table S5). Figure 5(D) presents the ground truth of neural connectomes in a directed graph, which was detected by electron microscopy in references (37, 39, 40). We calculated the IEE between different clusters to infer the IntDC network. The ROC curve of IEE is shown in Fig. 5(F) with an AUC value 0.882. The maximum Youden index, maximum concordance probability, and minimum distance to the point (0, 1) gave the same optimal operating point (OOP). At the OOP, Fig. 5(E) displays the inferred connectomic network by IEE. Comparisons with other ObsDC indices, i.e. GC/TE/CCM, revealed that IEE exhibited the highest AUC value, best OOP, largest similarity to the ground truth, lowest false positive at the OOP, and lowest false negative at the OOP (see Table 2, figs. S8-S10, and table S6). These findings demonstrate the efficacy of IEE in reconstructing the neural connectomes of *C. elegans*.

Application of IEE to COVID-19 transmission in Japan

We validated that IEE was a promising indicator for assessing the transmission dynamics of infectious diseases. Our study collected the daily confirmed COVID-19 cases from all 47 prefectures in Japan, spanning a duration of 1209 days from January 16, 2020 to May 8, 2023 (fig. S11).

First, we calculated the IEE indices for IntDC among different prefectures. IEE effectively ranked the influence across prefectures, with the top five affected areas by Tokyo being Kanagawa, Chiba, Saitama, Aichi, and Osaka. Remarkably, this ranking coincides with the geographical proximity and socio-economic connections to Tokyo. Kanagawa, Chiba and Saitama are in the same metropolitan area with Tokyo, while Aichi and Osaka are far from Tokyo but connected to Tokyo by expressway and Shinkansen.

Then, IEE was validated to coincide with the effective distance matrix D^{COVID} between prefectures. The $D^{\text{COVID}} \in \mathbb{R}^{47 \times 47}$ was non-symmetric and designed by incorporating factors such as geometric distances, human mobility, population sizes, and infectious rates across prefectures (based on the gravity model (41, 42), see Supplementary Text and fig. S11 for details). The element D_{ij}^{COVID} served as a benchmark for quantifying COVID-19 transmission from prefecture i to j . The IEE values demonstrated a strong linear correlation with $\ln D^{\text{COVID}}$, particularly when assessing the causality from Tokyo/Osaka to other prefectures (Figs. 6(A-B)). This correlation remained significant for other regions such as Aichi, Hokkaido, Fukuoka, and Okinawa (see fig. S12).

Further, IEE outperformed ObsDC indices in practicality. Notably, the absolute value of the Pearson correlation coefficient (PCC) between IEE and $\ln D^{\text{COVID}}$ was 0.724 substantially higher than those obtained by GC 0.161, TE 0.284, and CCM 0.568 (average over specific prefecture, see the second to last column in Table 3 and the boxplot in Fig. 6(C)). Table 3 presented more detailed comparisons to support the effectiveness of IEE (with Tokyo for specific

illustration in fig. S13).

These results underscore the reliability and efficacy of IEE in providing quantitative insights into COVID-19 transmission dynamics in Japan. Importantly, IEE performs as a simple and valuable tool for causal analyses solely from daily confirmed time-series data, without the need for complex models considering various factors such as geodesic distances, human mobility, population sizes, and infectious rates.

Application of IEE to investigating circadian rhythms

We investigated the gene regulatory networks (GRNs) related to key genes on the circadian rhythm. The time series of gene expressions were measured by microarray from cultured rat cells (43, 44). Through decades of molecular and genetic studies, many key circadian genes, such as *Clock*, *Bmal1*(*Arntl*), *Dec1*(*Bhlhb2*), *Dec2*(*Bhlhb3*), *Cry1*, *Cry2*, *Per1*, *Per2*, *Per3*, have been identified on mammals (45, 46). Figure 6(D) displayed the GRN around *Clock* at the protein level, where the transcription factor *Clock* is phosphorylated by PFK family genes. The ROC curves and AUC values for IEE/GC/TE/CCM were showed in Fig. 6(E). IEE designed for quantifying IntDC presented a higher AUC value (0.737) than ObsDC indices (0.490 for GC, 0.610 for TE, and 0.644 for CCM). In fig. S14, we also tested the indices on the GRN surrounding *Cry1/Cry2*, where IEE outperformed the others.

Concluding remarks and perspective

In summary, we have established a framework of IntDC based on dynamical systems theory and introduced the IEE criterion to quantify IntDC in this study. IEE measures the information flow between interventional causes and effects in the delay-embedding space, making it suitable for analyzing non-linear and non-separable systems (10, 14). Moreover, IEE is able to infer IntDC solely from observational time-series data, without requiring additional perturbations to

the system. This property makes IEE particularly suitable for non-intervention systems. Both theoretical derivations and numerical examples presented in this study provide strong evidence to support the high effectiveness, accuracy and robustness of IEE in detecting IntDC and reconstructing networks. Furthermore, IEE serves as an effective tool for evaluating and ranking the causal dependence between variables within a dynamical system. Through real-world examples, we illustrated the promising applicability of IEE in diverse fields such as regulatory inference and disease transmission studies.

There are several compelling issues that warrant further investigation and future development.

(1) The theory of IntDC and the IEE criterion can be extended to analyze causal relations between groups of variables. Specifically, in Eq. (6), the variables x and y can be generalized to high-dimensional vectors, enabling the investigation of complex interactions among multiple variables.

(2) The data in computing IEE can be non-uniformly sampled in the temporal space. We used the time-delayed embedding Eq. (2) and Eq. (3) in this paper, while according to the general Takens' embedding theorem, any $L + 1$ observations of x_t and y_t can form a topological diffeomorphism to \mathcal{M}_X and \mathcal{M}_Y , respectively. Equation (6) shows that only neighbors in the embedding space matter. Thus, IEE algorithm can be extended to infer causality using diverse datasets sampled at different intervals.

(3) To distinguish direct and indirect causality, we can generalize IEE to its conditional version

$$\text{cIEE}[x \rightarrow y|z] = \text{CMI}(\delta \mathbf{X}_t, \delta \mathbf{Y}_{t+1} | \mathbf{Y}_{t+1}, \mathbf{Z}_t, \delta \mathbf{Z}_t), \quad (10)$$

where “cIEE” is short for the conditional IEE, z is a third variable whose time-delay vector is \mathbf{Z}_t , and $\delta \mathbf{Z}_t$ represents the intervened deviation on \mathbf{Z}_t . Equation (10) measures the direct IntDC from x to y conditioned on z . Further, together with the well-known PC algorithm (47), cIEE is

one feasible way to remove high-order indirect causal edges iteratively and get the direct causal network.

(4) Moreover, causal inference with deep learning technology represents a frontier in research. Notable works include CausalEGM (48) and Causalformer (49). Combining IntDC and neural networks is a promising field. Causality theory brings interpretability for artificial intelligence, while big model can provide new discoveries in causal relationships. We are now entering a brilliant “big causality era”.

References

1. J. S. Neyman, *Statistical Science* **5**, 465 (1990).
2. D. B. Rubin, *The Annals of Statistics* **6**, 34 (1978).
3. J. S. Sekhon, *The Oxford Handbook of Political Methodology* **2**, 1 (2008).
4. S. Wright, *Journal of Agricultural Research* **20**, 557 (1921).
5. S. Wright, *The Annals of Mathematical Statistics* **5**, 161 (1934).
6. J. Pearl, *Biometrika* **82**, 669 (1995).
7. J. Pearl, *Statistics Surveys* **3**, 96 (2009).
8. J. Pearl, *Causality: models, reasoning, and inference* (Cambridge University Press, UK, 2000).
9. J. D. Angrist, G. W. Imbens, D. B. Rubin, *Journal of the American Statistical Association* **91**, 444 (1996).
10. J. Shi, L. Chen, K. Aihara, *Journal of the Royal Society Interface* **19**, 20210766 (2022).

11. C. W. J. Granger, *Econometrica* **37**, 424 (1969).
12. B. Lusch, P. D. Maia, J. N. Kutz, *Physical Review E* **94**, 032220 (2016).
13. T. Schreiber, *Physical Review Letters* **85**, 461 (2000).
14. G. Sugihara, *et al.*, *Science* **338**, 496 (2012).
15. S. Leng, *et al.*, *Nature Communications* **11**, 1 (2020).
16. X. Ying, *et al.*, *Research* **2022**, 9870149 (2022).
17. H. Ye, E. R. Deyle, L. J. Gilarranz, G. Sugihara, *Scientific Reports* **5**, 14750 (2015).
18. L. M. Pecora, T. L. Carroll, J. F. Heagy, *Physical Review E* **52**, 3420 (1995).
19. D. Harnack, E. Laminski, M. Schünemann, K. R. Pawelzik, *Physical Review Letters* **119**, 098301 (2017).
20. J. M. Amigó, Y. Hirata, *Chaos: An Interdisciplinary Journal of Nonlinear Science* **28**, 075302 (2018).
21. S. K. Stavroglou, A. A. Pantelous, H. E. Stanley, K. M. Zuev, *Proceedings of the National Academy of Sciences U.S.A.* **117**, 7599 (2020).
22. P. Tao, *et al.*, *Fundamental Research* (2023).
23. G. Stepaniants, B. W. Brunton, J. N. Kutz, *Physical Review E* **102**, 042309 (2020).
24. D. A. Smirnov, *Physical Review E* **90**, 062921 (2014).
25. D. A. Smirnov, *Physical Review E* **102**, 062139 (2020).

26. F. Takens, *Dynamical systems and turbulence, Warwick 1980* (Springer, 1981), pp. 366–381.
27. T. Sauer, J. A. Yorke, M. Casdagli, *Journal of Statistical Physics* **65**, 579 (1991).
28. J. Stark, D. Broomhead, M. Davies, J. Huke, *Nonlinear Analysis: Theory, Methods and Applications* **30**, 5303 (1997).
29. B. Cummins, T. Gedeon, K. Spendlove, *SIAM Journal on Applied Dynamical Systems* **14**, 335 (2015).
30. N. Altman, M. Krzywinski, *Nature methods* **12** (2015).
31. A. Shojaie, E. B. Fox, *Annual Review of Statistics and Its Application* **9**, 289 (2022).
32. K. B. Korb, L. R. Hope, A. E. Nicholson, K. Axnick, *PRICAI 2004: Trends in Artificial Intelligence* (Springer, 2004), pp. 322–331.
33. P.-O. Amblard, O. J. Michel, *Entropy* **15**, 113 (2012).
34. T. M. Cover, *Elements of information theory* (John Wiley & Sons, 1999).
35. K. Aihara, T. Takabe, M. Toyoda, *Physics Letters A* **144**, 333 (1990).
36. M. Adachi, K. Aihara, *Neural Networks* **10**, 83 (1997).
37. S. J. Cook, *et al.*, *Nature* **571**, 63 (2019).
38. S. Kato, *et al.*, *Cell* **163**, 656 (2015).
39. A. Banerjee, S. Chandra, E. Ott, *Proceedings of the National Academy of Sciences U.S.A.* **120**, e2216030120 (2023).

- 40. Emmons Lab, Hermaphrodite and Male Connectomes (Adjacency Matrices), Adults (corrected July 2020), available at <https://wormwiring.org/pages/adjacency.html> (2020). Accessed: 2023-12-15.
- 41. H. Barbosa, *et al.*, *Physics Reports* **734**, 1 (2018).
- 42. G. K. Zipf, *American Sociological Review* **11**, 677 (1946).
- 43. Y. Wang, X.-S. Zhang, L. Chen, *OMICS* **13**, 313 (2009).
- 44. S. Kawaguchi, *et al.*, *Biochemical and Biophysical Research Communications* **355**, 555 (2007).
- 45. C. H. Ko, J. S. Takahashi, *Human Molecular Genetics* **15**, R271 (2006).
- 46. H. R. Ueda, *et al.*, *Nature Genetics* **37**, 187 (2005).
- 47. P. Spirtes, C. Glymour, *Social Science Computer Review* **9**, 62 (1991).
- 48. Q. Liu, Z. Chen, W. H. Wong, *arXiv preprint arXiv:2212.05925* (2022).
- 49. Z. Lu, *et al.*, *arXiv preprint arXiv:2311.06928* (2023).

Acknowledgments

Funding:

This work was supported by the National Key R&D Program of China 2022YFC2704604, the National Natural Science Foundation of China No. 12301620 and No. 32100509, the Moonshot R&D Grant Number JPMJMS2021, Institute of AI and Beyond of UTokyo, the International Research Center for Neurointelligence (WPI-IRCIN) at The University of Tokyo Institutes for Advanced Study (UTIAS), JSPS KAKENHI Grant Number JP20H05921, the Cross-

ministerial Strategic Innovation Promotion Program (SIP), and the 3rd period of SIP “Smart energy management system” Grant Number JPJ012207.

Author contributions:

Conceptualization: J.S., K.A., L.C., and W.L.

Methodology: J.S., K.A., L.C., and W.L.

Investigation: J.S., Y.L., J.Z., and S.L.

Visualization: J.S., Y.L., J.Z., S.L.

Supervision: K.A., L.C., and W.L.

Writing – original draft: J.S., Y.L., J.Z., and L.C.

Writing – review & editing: All authors.

Competing interests:

The authors declare no competing interest.

Data and materials availability:

The code for IEE is available at <https://github.com/smsxiaomayi/IEE>.

Supplementary materials

Materials and Methods

Supplementary Text

Figs. S1 to S14

Tables S1 to S6

References

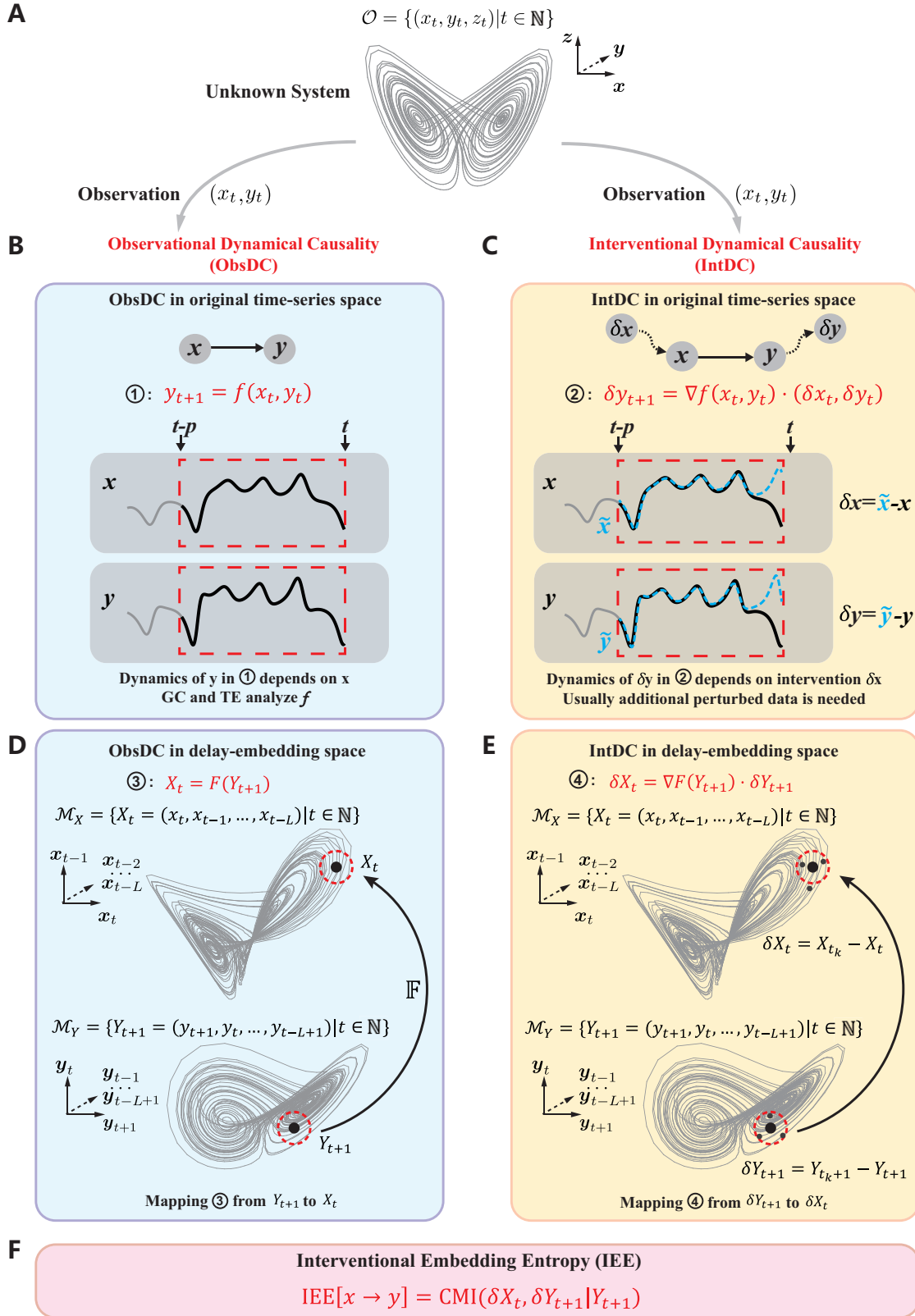


Figure 1: Illustration for the observational dynamical causality (ObsDC) and interventional dynamical causality (IntDC). (A) An illustrative example of a complex system where (x_t, y_t) are observed time series. The z_t stands for the unobserved variable. (B) ObsDC from x to y indicates that the dynamics of y depends on x . Algorithms such as Granger causality (GC) and transfer entropy (TE) infer the ObsDC in the original time-series space. (C) IntDC from x to y indicates that the deviation of y , i.e. δy , depends on an intervention on x , i.e. δx . Usually additional data from a perturbed system $(\tilde{x}_t, \tilde{y}_t)$ is necessary for detecting IntDC. (D) ObsDC can be detected in the embedding space by cross mapping \mathbb{F} . The causal vector X_t can be reconstructed by the effect vector Y_{t+1} . (E) IntDC can be modeled in the embedding space. The interventional causal vector δX_t should be reconstructable by the effect vector δY_{t+1} around Y_{t+1} . The δY_{t+1} is approximated by the distance from Y_{t+1} to its neighbors Y_{t_k+1} , while δX_t is obtained by X_{t_k} with the same time label t_k . (F) Interventional embedding entropy (IEE) measures the average information retention contained in δY_{t+1} from δX_t , quantifying the IntDC from variable x to y . Notably, IEE does not require additional perturbations to the system and can be inferred from observational data solely.

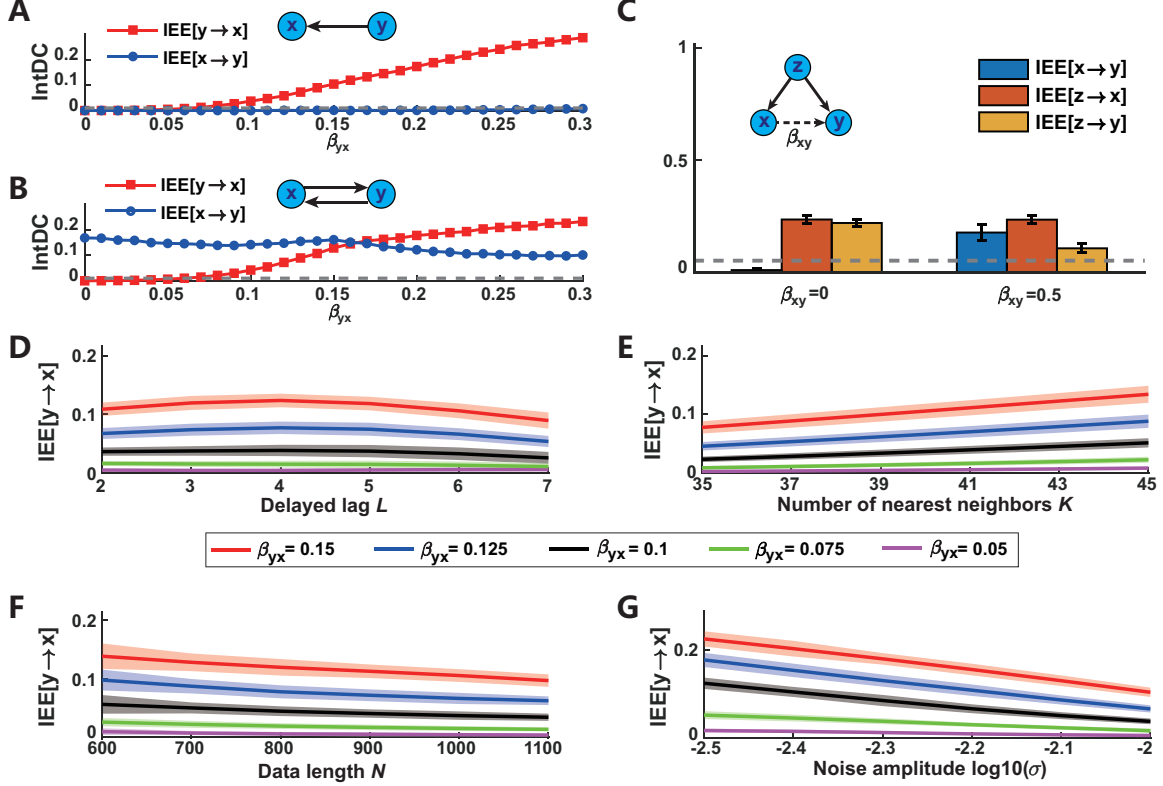


Figure 2: Performance of IEE on the Logistic systems. (A) and (B) used the two-node Logistic system. The β_{xy} and β_{yx} control the coupling coefficients from x to y and from y to x , respectively. (A) shows the mean values of IEE when $\beta_{xy} = 0$ and β_{yx} ranges from 0 to 0.3 over 100 simulations. $IEE[y \rightarrow x]$ (the red line with squares) increases monotonically, while $IEE[x \rightarrow y]$ (the blue line with dots) stays around zero. (B) is under $\beta_{xy} = 0.1$, in which $IEE[x \rightarrow y]$ (the blue line with dots) is significantly positive. The gray dashed lines in (A) and (B) represent the constant 0.01 as reference. (C) shows the performance of IEE in the three-node Logistic system, where z acts as a confounding variable. When $\beta_{xy} = 0$, $IEE[x \rightarrow y]$ is almost zero correctly. IEE designed for measuring IntDC is not affected by confounders, which usually leads to false positives. The results for $\beta_{xy} = 0.5$ is shown for a comparison. The gray dashed line is 0.05 for reference. (D-G) demonstrate the robustness of IEE under different delayed lags L , the numbers of nearest neighbors K , data lengths N , and noise amplitudes σ in the two-node logistic system, respectively. The parameter $\beta_{xy} \equiv 0$, and β_{yx} takes values of 0.15 (red), 0.125 (blue), 0.1 (black), 0.075 (green), and 0.05 (magenta). Lines denote mean values under 50 simulations, and shaded areas represent the standard deviation. IEE maintains correct orders of IntDC under different situations with relatively stable variations.

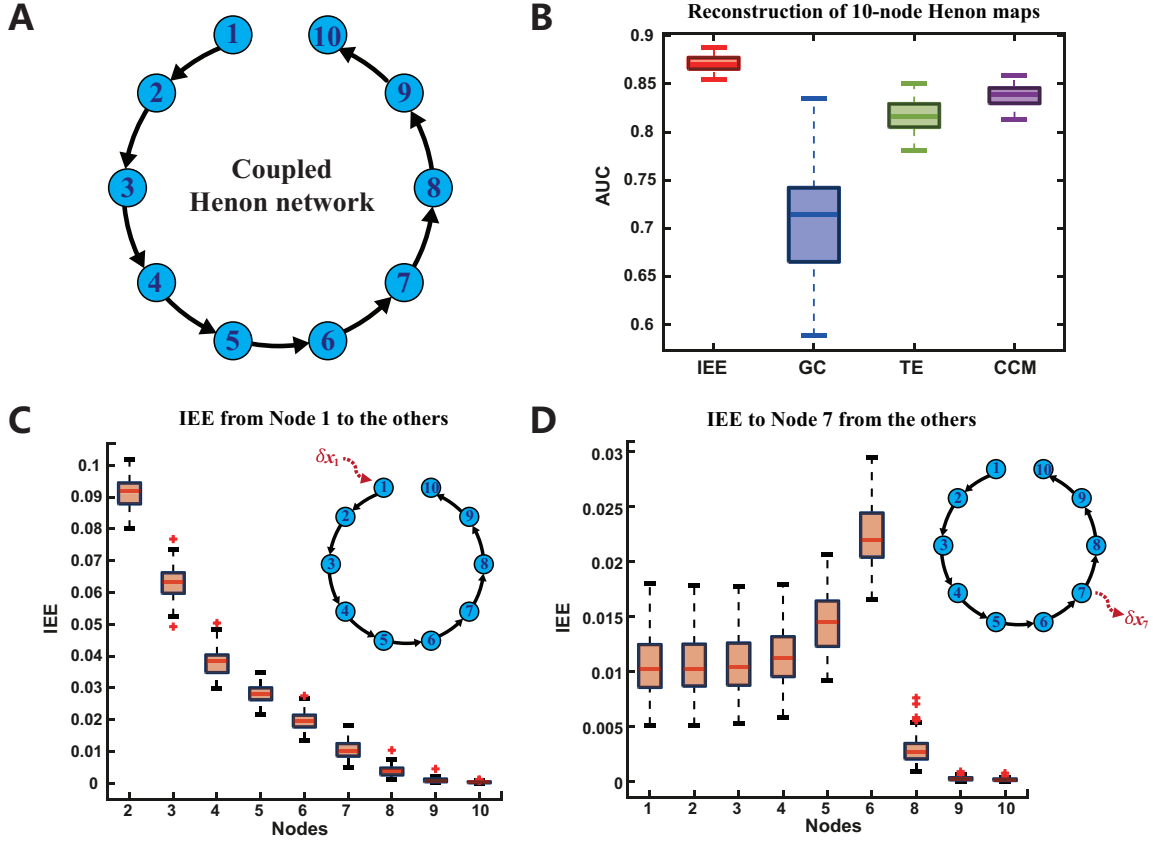


Figure 3: Performance of IEE on the 10-node coupled Henon-map dynamics. (A) illustrates the network structure of the dynamics. There are directed causality from each node to its subsequent node. (B) presents a boxplot of the Area Under Curve (AUC) values for the network reconstruction. IEE outperforms GC, TE, and CCM significantly in accuracy and stability. (C) demonstrates the IEE from Node 1 to the other nine nodes, while (D) shows the IEE received by Node 7 from the other nodes. IEE accurately captures the interventional flow and IntDC in cascade topology.

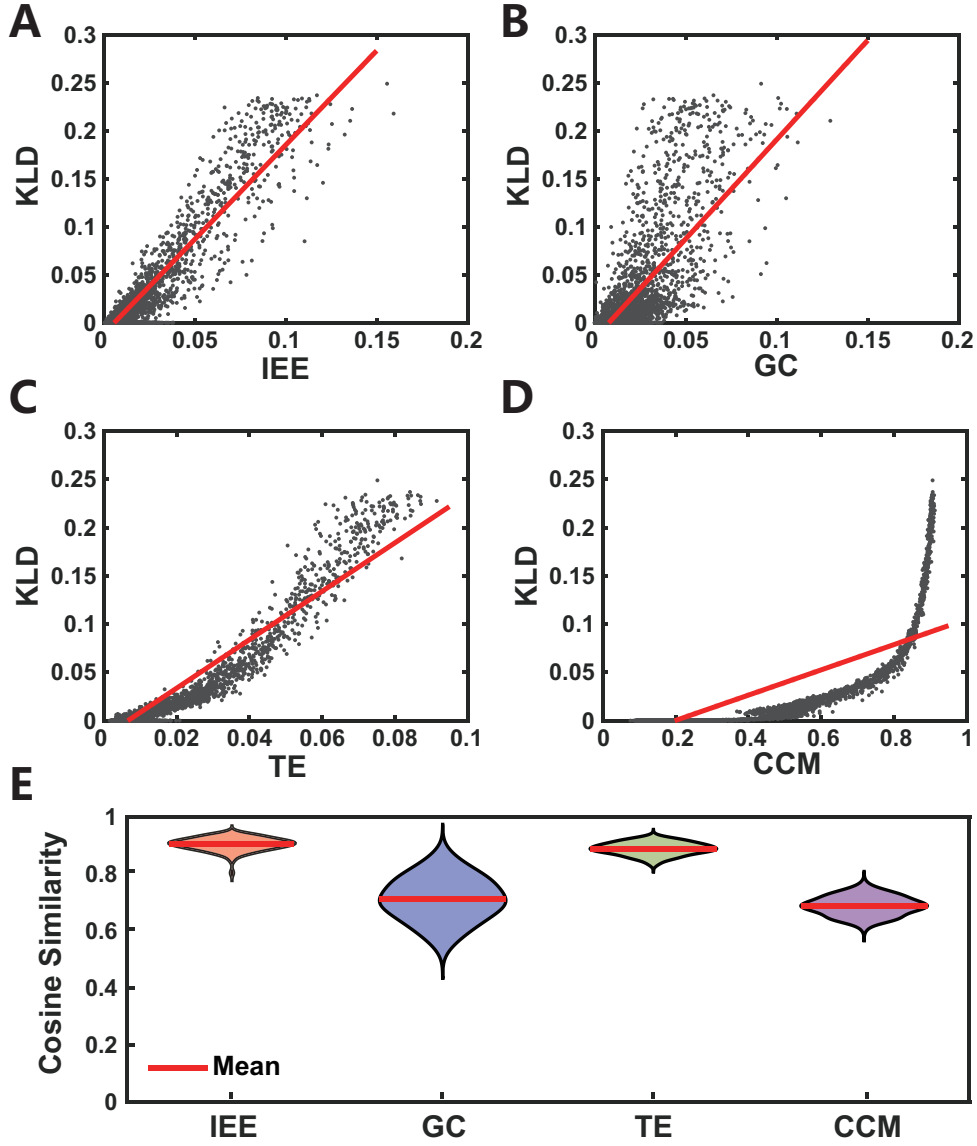


Figure 4: The performance of IEE when measuring the influence of perturbations on the chaotic neural networks (chNNs). The Kullback-Leibler divergence (KLD) is utilized to measure the true influence or IntDC between neurons. In (A-D), 1000 samples for different perturbations on chNNs are represented by gray dots, along with the linear regressions (the red lines) between KLD and IEE/GC/TE/CCM, respectively. (E) displays the violin plots of cosine similarity between KLD and IEE/GC/TE/CCM. The mean values and standard variations of the cosine similarity are IEE (0.904 ± 0.024), GC (0.711 ± 0.076), TE (0.888 ± 0.022), and CCM (0.687 ± 0.033). IEE can linearly reflect the KLD with high similarity, indicating its effectiveness in accurately quantifying IntDC without additional perturbed data on chNNs.

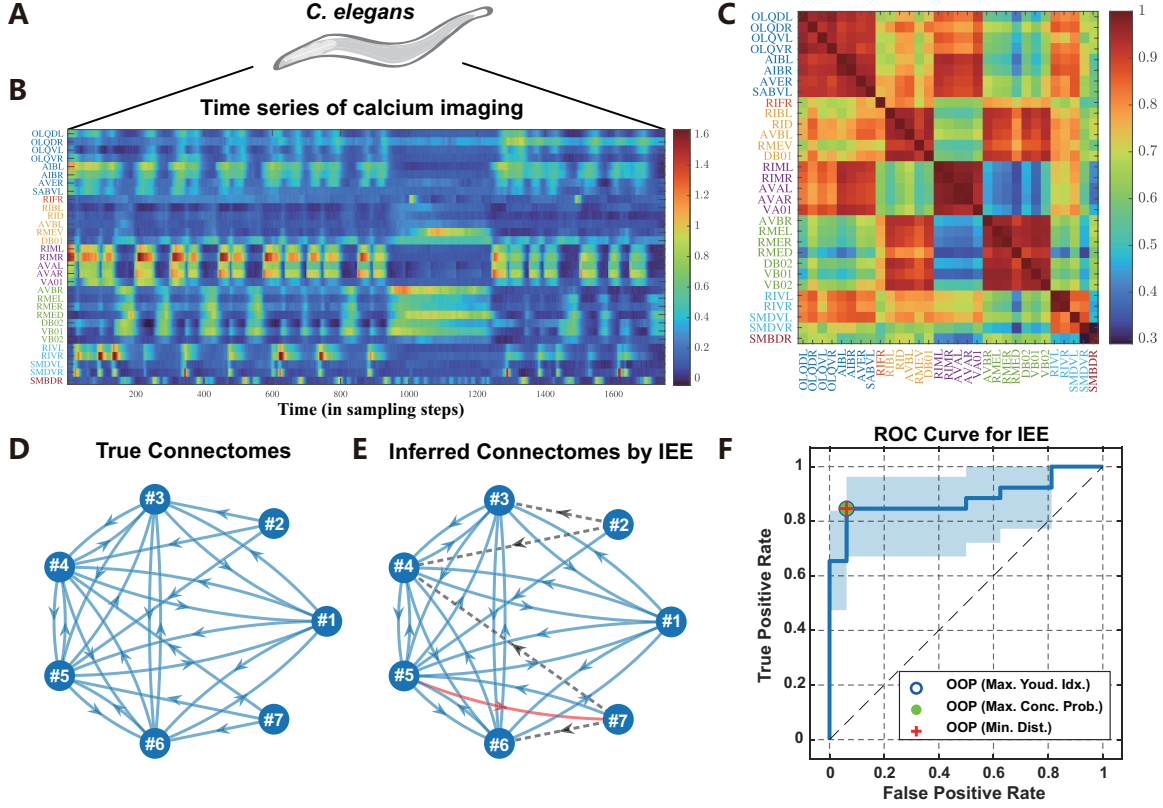


Figure 5: Application of the IEE on inferring the neural connectomes of *C. elegans*. (A) is an illustration of *C. elegans*. (B) displays the calcium imaging time series of 31 key neurons, with their names listed on the left and colors representing different clusters. (C) is the cosine similarity matrix between neurons, aiding the clustering process. (D) is the true connectomes between 7 clusters, while (E) is the inferred causal network at the the optimal operating point (OOP) determined by IEE. The red edge represents a false positive, and the black dashed edges represent false negatives. (F) shows the ROC curve (the blue line) for IEE. The same OOP is obtained under three criteria, i.e. the maximum Youden index (the blue circle), the maximum concordance probability (the green dot), and the minimum distance to the point (0, 1) (the red cross). The shaded area around the ROC curve represents the 95% confidence interval obtained through bootstrapping. The AUC value of IEE is 0.882.

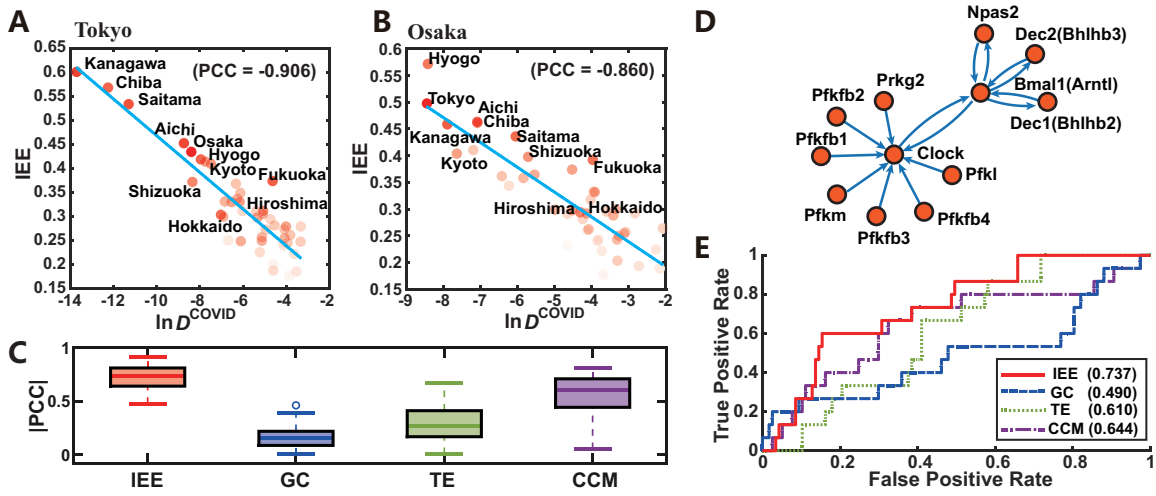


Figure 6: Application of the IEE on the COVID-19 transmission in Japan and the gene regulatory network (GRN) of circadian rhythms. (A) shows that IEE values from Tokyo to other prefectures are highly linear-correlated with $\ln D^{\text{COVID}}$, where D^{COVID} is the effective distance obtained from the gravity model in consideration of various factors. (B) is the result for IEE values from Osaka to the other prefectures. (C) is the boxplot for $|\text{PCC}(c_{ij}^{\text{Inf}}, \ln D_{ij}^{\text{COVID}})|$ with average over fixed i , where PCC is the Pearson correlation coefficient and c^{Inf} is the inferred causal strengths by IEE, GC, TE, or CCM. The PCC linearity of IEE (0.724 ± 0.116) is significantly higher than that of GC (0.161 ± 0.099), TE (0.284 ± 0.168), and CCM (0.568 ± 0.174). (D) shows the GRN surrounding *Clock*, a key circadian gene. (E) demonstrates the ROC curves and AUC values of the IntDC index IEE, and three ObsDC indices GC/TE/CCM.

Table 1: Algorithm: Interventional Embedding Entropy (IEE).

1. Given observed time series $\{x_{t_n}|t_n \geq 0\}, \{y_{t_n}|t_n \geq 0\}$.
2. Construct time-delay vectors \mathbf{X}_{t_n} and $\mathbf{Y}_{t_{n+1}}$ by Eqs. (2)-(3).
3. Get K nearest neighbors $\mathbf{Y}_{t_{k+1}}$ around $\mathbf{Y}_{t_{n+1}}, k = 1, 2, \dots, K$.
4. Sample $\delta \mathbf{Y}_{t_{n+1}}$ condition on $\mathbf{Y}_{t_{n+1}}$ as $\mathbf{Y}_{t_{k+1}} - \mathbf{Y}_{t_n}$.
5. Sample $\delta \mathbf{X}_{t_n}$ condition on $\mathbf{Y}_{t_{n+1}}$ as $\mathbf{X}_{t_k} - \mathbf{X}_{t_n}$.
6. Calculate Eq. (6) around $\mathbf{Y}_{t_{n+1}}$ and average over n to approximate $\text{IEE}[x \rightarrow y]$.

Table 2: Comparison of causal indices on the inference of *C. elegans* neural connectomes.

	Properties of ROC curves				Cosine Similarity	
	AUC	Maximum Youden index	Maximum concordance probability	Minimum distance to (0, 1)	to \mathbf{C}	to $\log(1 + \mathbf{C})$
\mathbf{C}^{IEE}	0.882	0.784	0.793	0.166	0.750	0.905
\mathbf{C}^{GC}	0.858	0.721	0.740	0.198	0.430	0.678
\mathbf{C}^{TE}	0.796	0.620	0.656	0.269	0.477	0.726
\mathbf{C}^{CCM}	0.880	0.615	0.639	0.294	0.644	0.866

* The matrices $\mathbf{C}^{\text{IEE}}/\mathbf{C}^{\text{GC}}/\mathbf{C}^{\text{TE}}/\mathbf{C}^{\text{CCM}}$ represent the inferred connectomes by the four indices. The matrix \mathbf{C} is the ground truth of neural connectomes. The best value in each column is shown in bold.

Table 3: Comparison of IEE/GC/TE/CCM in measuring causal strengths in the transmission of COVID-19 data in Japan.

	PCC ($c_{ij}^{\text{Inf}}, \ln D_{ij}^{\text{COVID}}$) for specific prefecture (fixed i)							PCC ($c_{ij}^{\text{Inf}}, \ln D_{ij}^{\text{COVID}}$) for all i, j with $i \neq j$
	Tokyo ($i = 13$)	Osaka ($i = 27$)	Aichi ($i = 23$)	Hokkaido ($i = 1$)	Fukuoka ($i = 40$)	Okinawa ($i = 47$)	Average over all i	
IEE	0.906	0.860	0.811	0.751	0.752	0.811	0.724	0.748
GC	0.462	0.387	0.236	0.070	0.125	0.164	0.161	0.166
TE	0.655	0.308	0.018	0.445	0.526	0.538	0.284	0.109
CCM	0.799	0.795	0.448	0.052	0.727	0.477	0.568	0.585

* i and j (ranging from 1 to 47) stand for different prefectures in Japan. c_{ij}^{Inf} is the causal strength from the prefecture i to j inferred by IEE, GC, TE, or CCM. D_{ij}^{COVID} is the effective distance between prefectures i and j . PCC is the Pearson correlation coefficient. The best value in each column is shown in bold.

Supplementary Materials for

Deciphering interventional dynamical causality from non-intervention systems

Jifan Shi, Yang Li, Juan Zhao, Siyang Leng, Kazuyuki Aihara, Luonan Chen,
Wei Lin

Corresponding authors: kaihara@g.ecc.u-tokyo.ac.jp (K.A.), lnchen@sibs.ac.cn (L.C.),
wlin@fudan.edu.cn (W.L.).

The PDF file includes:

Materials and Methods
Supplementary Text
Supplementary figs. S1 to S14
Supplementary tables S1 to S6
References

1 Materials and Methods

The calcium fluorescence imaging data of *C. elegans* was collected from (1), and the neural connectomes were available in (2–4). The daily confirmed COVID-19 cases of 47 prefectures in Japan (1209 days) were obtained from the website of the Ministry of Health, Labour and Welfare of Japan (5). To construct the effective distance matrix, the geodesic distances between prefectures were collected from (6). The net and gross human mobility data were from (7) and (8), respectively. The population counts of each prefecture were from the statistics bureau of Japan (9). The circadian rhythm dataset was collected from (10, 11).

2 Supplementary Text

2.1 Derivation of Eq. (4) in the maintext

Denote \mathcal{O} as the attractive manifold of $\{\mathbf{m}_{x,y}(t) = (x_t, x_{t-1}, \dots, x_{t-p}, y_t, y_{t-1}, \dots, y_{t-p})^T | t \geq 0\}$ when $t \rightarrow +\infty$. Because the dynamics of x is autonomous, we denote \mathcal{O}_X as the attractive manifold of $\{\mathbf{m}_x(t) = (x_t, x_{t-1}, \dots, x_{t-p})^T | t \geq 0\}$ when $t \rightarrow +\infty$. The topological spaces formed by the noise terms are denoted as $\Sigma_{X,Y} = \{\boldsymbol{\varepsilon}_{x,y,t} = (\varepsilon_{x,t}, \dots, \varepsilon_{x,t-p}, \varepsilon_{y,t}, \dots, \varepsilon_{y,t-p})^T | t \geq 0\}$ and $\Sigma_X = \{\boldsymbol{\varepsilon}_{x,t} = (\varepsilon_{x,t}, \varepsilon_{x,t-1}, \dots, \varepsilon_{x,t-p})^T | t \geq 0\}$. Using the notations in Methods section in the main text and according to the seminal stochastic version of Takens' embedding theorem (12–15), for open dense sets $\boldsymbol{\varepsilon}_x \subseteq \Sigma_X$, $\boldsymbol{\varepsilon}_{x,y} \subseteq \Sigma_{X,Y}$ and delay dimension $L \geq 2d$, we can obtain

$$\mathbf{X}_t = \varphi_X^{\boldsymbol{\varepsilon}_x}(\mathbf{m}_x(t)), \quad (\text{S1})$$

$$\mathbf{Y}_{t+1} = \varphi_Y^{\boldsymbol{\varepsilon}_{x,y}}(\mathbf{m}_{x,y}(t)), \quad (\text{S2})$$

where $\varphi_X^{\boldsymbol{\varepsilon}_x} : \mathcal{O}_X \rightarrow \mathcal{M}_X$ and $\varphi_Y^{\boldsymbol{\varepsilon}_{x,y}} : \mathcal{O} \rightarrow \mathcal{M}_Y$ are diffeomorphisms in the generic sense, i.e. $\varphi_X^{\boldsymbol{\varepsilon}_x}$ and $\varphi_Y^{\boldsymbol{\varepsilon}_{x,y}}$ are one-to-one with differentiable inverse mappings. By definition, the mapping $\Pi : \mathbf{m}_{x,y}(t) \mapsto \mathbf{m}_x(t)$ is a projection. Together with Eqs. (S1) and (S2), we can derive

$$\mathbf{X}_t = \mathbf{F}_{\boldsymbol{\varepsilon}_{x,y}}(\mathbf{Y}_{t+1}), \quad (\text{S3})$$

where $\mathbf{F}_{\boldsymbol{\varepsilon}_{x,y}} = \varphi_X^{\boldsymbol{\varepsilon}_x} \circ \Pi \circ (\varphi_Y^{\boldsymbol{\varepsilon}_{x,y}})^{-1}$. For simplicity, we use the notation \mathbf{F} in Eq. (4) in the maintext. The irreversibility of \mathbf{F} is due to the projection operation Π .

2.2 Numerical algorithm for IEE

The interventional embedding entropy (IEE) criterion from x to y is

$$\text{IEE}[x \rightarrow y] = \text{CMI}(\delta \mathbf{X}_t, \delta \mathbf{Y}_{t+1} | \mathbf{Y}_{t+1}), \quad (\text{S4})$$

where $\mathbf{X}_t, \mathbf{Y}_{t+1}$ are delay-embedding vectors, and $\delta\mathbf{X}_t, \delta\mathbf{Y}_{t+1}$ are corresponding deviations caused by interventions. To numerically approximate Eq. (S4) solely from the observed data, we have

$$\begin{aligned}
& \text{IEE}[x \rightarrow y] \\
&= \iiint p(\mathbf{Y}_{t+1}) p(\delta\mathbf{X}_t, \delta\mathbf{Y}_{t+1} | \mathbf{Y}_{t+1}) \log \frac{p(\delta\mathbf{X}_t, \delta\mathbf{Y}_{t+1} | \mathbf{Y}_{t+1})}{p(\delta\mathbf{X}_t | \mathbf{Y}_{t+1}) p(\delta\mathbf{Y}_{t+1} | \mathbf{Y}_{t+1})} d\delta\mathbf{X}_t d\delta\mathbf{Y}_{t+1} d\mathbf{Y}_{t+1} \\
&\approx \frac{1}{N} \sum_{n=1}^N \iint p(\delta\mathbf{X}_{t_n}, \delta\mathbf{Y}_{t_n+1} | \mathbf{Y}_{t_n+1}) \log \frac{p(\delta\mathbf{X}_{t_n}, \delta\mathbf{Y}_{t_n+1} | \mathbf{Y}_{t_n+1})}{p(\delta\mathbf{X}_{t_n} | \mathbf{Y}_{t_n+1}) p(\delta\mathbf{Y}_{t_n+1} | \mathbf{Y}_{t_n+1})} d\delta\mathbf{X}_{t_n} d\delta\mathbf{Y}_{t_n+1} \\
&= \frac{1}{N} \sum_{n=1}^N \text{MI}(\delta\mathbf{X}_{t_n} | \mathbf{Y}_{t_n+1}, \delta\mathbf{Y}_{t_n+1} | \mathbf{Y}_{t_n+1}), \tag{S5}
\end{aligned}$$

where N is the total number of points in the delayed-embedding space, $\delta\mathbf{Y}_{t_n+1} | \mathbf{Y}_{t_n+1}$ is sampled as $\mathbf{Y}_{t_k+1} - \mathbf{Y}_{t_n+1}$ representing the interventional effect around \mathbf{Y}_{t_n+1} , \mathbf{Y}_{t_k+1} is the k th nearest neighbor of \mathbf{Y}_{t_n+1} in the embedding space, $\delta\mathbf{X}_{t_n} | \mathbf{Y}_{t_n+1}$ is sampled as $\mathbf{X}_{t_k} - \mathbf{X}_{t_n}$ with the same time label t_k representing the interventional cause around \mathbf{X}_{t_n} , and MI is the mutual information

$$\text{MI}(\mathbf{x}, \mathbf{y}) = \iint p(\mathbf{x}, \mathbf{y}) \log \frac{p(\mathbf{x}, \mathbf{y})}{p(\mathbf{x})p(\mathbf{y})} d\mathbf{x} d\mathbf{y}, \tag{S6}$$

which can be realized by the kNN algorithm in high dimensional cases (16–18). We used the symbol t_k instead of $t_k^{(n)}$ for simplicity, but we should remember that the time labels for nearest neighbors change for different points \mathbf{Y}_{t_n+1} . Table 1 in the main text lists steps for the IEE algorithm, and the code is available at <https://github.com/smsxiaomay/IEE>.

2.3 Two-node Logistic dynamics

The two-node Logistic dynamics is

$$\begin{cases} x_{t+1} = 3.7[(1 - \beta_{yx})x_t(1 - x_t) + \beta_{yx}y_t(1 - y_t)] + \varepsilon_{x,t}, \\ y_{t+1} = 3.7y_t[1 - (1 - \beta_{xy})y_t - \beta_{xy}x_t] + \varepsilon_{y,t}, \end{cases} \tag{S7}$$

where parameter β_{xy} adjusts the causality from x to y , β_{yx} controls the causality from y to x , and $\varepsilon_{x,t}, \varepsilon_{y,t}$ are independent Gaussian variables representing the noise.

In Fig. 2(A) in the main text, we set $\beta_{yx} \equiv 0$ and let β_{yx} change from 0 to 0.30. When $\beta_{yx} \neq 0$, there is no IntDC from x to y while there exists unidirectional IntDC from y to x . For each β_{yx} , we simulated 100 trajectories, and calculated $\text{IEE}[y \rightarrow x]$ and $\text{IEE}[x \rightarrow y]$. Parameters were chosen as: data length $N = 1000$, delayed lag $L = 2$, number of nearest neighbors $K = 40$, and noise amplitude $\sigma = 0.01$. The same time series were used to calculate GC, TE, and CCM, whose results are shown in fig. S1. Table S1 shows mean values and

standard variations of the four causal indices from y to x under 100 simulations, and table S2 is for the causality from x to y .

In Fig. 2(B) in the main text, we set $\beta_{xy} \equiv 0.1$ and let β_{yx} change from 0 to 0.30. When $\beta_{yx} \neq 0$, there is bidirectional IntDC between x and y . For each β_{yx} , we simulated 100 trajectories, and calculated $\text{IEE}[y \rightarrow x]$ and $\text{IEE}[x \rightarrow y]$. Parameters were chosen as: data length $N = 1000$, delayed lag $L = 2$, number of nearest neighbors $K = 40$, and noise amplitude $\sigma = 0.01$. The same time series were used to calculate GC, TE, and CCM, whose results are shown in fig. S2. Table S3 shows mean values and standard variations of the four causal indices from y to x under 100 simulations, and table S4 is for the causality from x to y .

In Fig. 2(D) in the main text, we set $\beta_{xy} \equiv 0$ and let $\beta_{yx} = 0.15, 0.125, 0.1, 0.075, 0.05$. Delayed lag L changed from 2 to 7. For each β_{yx} and L , we simulated 50 trajectories and calculated $\text{IEE}[y \rightarrow x]$. Parameters were chosen as: data length $N = 1000$, number of nearest neighbors $K = 40$, and noise amplitude $\sigma = 0.01$.

In Fig. 2(E) in the main text, we set $\beta_{xy} \equiv 0$ and let $\beta_{yx} = 0.15, 0.125, 0.1, 0.075, 0.05$. Number of nearest neighbors K changed from 35 to 45. For each β_{yx} and K , we simulated 50 trajectories and calculated $\text{IEE}[y \rightarrow x]$. Parameters were chosen as: data length $N = 1000$, delayed lag $L = 2$, and noise amplitude $\sigma = 0.01$.

In Fig. 2(F) in the main text, we set $\beta_{xy} \equiv 0$ and let $\beta_{yx} = 0.15, 0.125, 0.1, 0.075, 0.05$. Data length N changed from 600 to 1100. For each β_{yx} and N , we simulated 50 trajectories and calculated $\text{IEE}[y \rightarrow x]$. Parameters were chosen as: delayed lag $L = 2$, number of nearest neighbors $K = 40$, and noise amplitude $\sigma = 0.01$.

In Fig. 2(G) in the main text, we set $\beta_{xy} \equiv 0$ and let $\beta_{yx} = 0.15, 0.125, 0.1, 0.075, 0.05$. Noise amplitude σ changed from $10^{-2.5}$ to 10^{-2} . For each β_{yx} and σ , we simulated 50 trajectories and calculated $\text{IEE}[y \rightarrow x]$. Parameters were chosen as: data length $N = 1000$, delayed lag $L = 2$, and number of nearest neighbors $K = 40$.

2.4 Three-node Logistic dynamics

We used a three-node Logistic dynamics to test the performance of IEE when there exists confounding variable. The dynamics is

$$\begin{cases} x_{t+1} = \gamma_x x_t [1 - (1 - \frac{\beta_{zx}}{\gamma_x}) x_t - \frac{\beta_{zx}}{\gamma_x} z_t] + \varepsilon_{x,t}, \\ y_{t+1} = \gamma_y y_t [1 - (1 - \frac{\beta_{xy} + \beta_{zy}}{\gamma_y}) y_t - \frac{\beta_{xy}}{\gamma_y} x_t - \frac{\beta_{zy}}{\gamma_y} z_t] + \varepsilon_{y,t}, \\ z_{t+1} = \gamma_z z_t (1 - z_t) + \varepsilon_{z,t}, \end{cases} \quad (\text{S8})$$

where $\gamma_x = \gamma_y = \gamma_z = 3.7$, noises $\varepsilon_{x,t}, \varepsilon_{y,t}, \varepsilon_{z,t}$ are independent Gaussian variables $\mathcal{N}(0, 0.001)$, β_{xy} adjusts the causal strength from x to y , and parameters $\beta_{zx} = \beta_{zy} = 0.5$ represent the causality from z to x and z to y , respectively. There are constant causality from z to x and from z to y , and z is a confounder. When $\beta_{xy} = 0$, we simulated 100 trajectories and calculated IEE, GC, TE, and CCM for edges $x \rightarrow y$, $z \rightarrow x$, and $z \rightarrow y$. When $\beta_{xy} = 0.5$, we did the same computation. Parameters were chosen as: data length $N = 1000$, delayed lag $L = 2$, number of

nearest neighbors $K = 20$. In fig. S3, we showed the results for the four indices, respectively. The result for IEE is also displayed in Fig. 2(C) in the main text. The causal strength from x to y were correct for IEE when $\beta_{xy} = 0$, while the GC/TE/CCM exhibited false positives in some degree. The gray dashed line is 0.05 for a reference.

2.5 10-node coupled Henon maps

The dynamics of the 10-node coupled Henon maps are

$$x_{i,t+1} = 1 - ax_{i,t}^2 + bx_{i,t-1} + \sigma\varepsilon_{i,t}, \quad i = 1, \quad (\text{S9a})$$

$$x_{i,t+1} = 1 - a(\beta x_{i-1,t} + (1 - \beta)x_{i,t})^2 + bx_{i,t-1} + \sigma\varepsilon_{i,t}, \quad i = 2, 3, \dots, 10, \quad (\text{S9b})$$

where parameters $a = 1.4$, $b = 0.3$ are constant, $\sigma = 0.002$ is the noise amplitude, noise term $\varepsilon_{i,t}$ are independent standard Gaussian random variables, and $\beta = 0.6$ is the coupling coefficient representing the causality from variable x_i to x_{i+1} . We sampled 500 time points for each trial from initial point $x_{i,1} = 0.5$, $i = 1, 2, \dots, 10$.

In Fig. 3(B) in the main text, we simulated 20 trials and calculated 20 AUC values for IEE, GC, TE, and CCM in reconstructing the network. ROC curves for one trial can be found in fig. S4. Parameters were chosen as: delayed lag $L = 2$, number of nearest neighbors $K = 10$.

In Fig. 3(C) in the main text, we simulated 100 trials and calculated the causal strength from node 1 to the other nine nodes. Results for GC, TE, and CCM can be found in fig. S5. Parameters were chosen as: delayed lag $L = 2$, number of nearest neighbors $K = 10$.

In Fig. 3(D) in the main text, we simulated 100 trials and calculated the causal strength received by node 7 from the other nine nodes. Results for GC, TE, and CCM can be found in fig. S6. Parameters were chosen as: delayed lag $L = 2$, number of nearest neighbors $K = 10$.

2.6 Chaotic neural networks

The chaotic neural network (chNN) is composed of N_{node} chaotic neurons, each of which is described by an output variable x_i and two internal state variables: a feedback state variable y_i , and a refractory state variable z_i (19, 20). The dynamics of chNN is given by

$$x_{i,t+1} = \tanh[s(y_{i,t+1} + z_{i,t+1})], \quad (\text{S10a})$$

$$y_{i,t+1} = k_f y_{i,t} + \beta \sum_{j=1}^{N_{\text{node}}} w_{ij} x_{j,t} + \sigma_f \varepsilon_{y_i,t}, \quad (\text{S10b})$$

$$z_{i,t+1} = k_r z_{i,t} - \alpha x_{i,t} + b_i + \sigma_r \varepsilon_{z_i,t}, \quad (\text{S10c})$$

where $i = 1, 2, \dots, N_{\text{node}}$, $s > 0$ is the steepness parameter, $k_f, k_r \in [0, 1)$ are decay parameters, α, β are coupling strengths, w_{ij} is the weight between x_j and y_i , $\mathbf{b} = (b_1, b_2, \dots, b_{N_{\text{node}}})^\top \in \mathbb{R}^{N_{\text{node}}}$ denotes bias, $\sigma_f, \sigma_r > 0$ are noise amplitudes, and $\varepsilon_{y_i,t}, \varepsilon_{z_i,t}$ are standard Gaussian noise terms. The dynamics can be written into a vector-matrix form

$$\begin{cases} \mathbf{x}_{t+1} &= \tanh(s(\mathbf{y}_{t+1} + \mathbf{z}_{t+1})), \\ \mathbf{y}_{t+1} &= k_f \mathbf{y}_t + \beta \mathbf{W} \mathbf{x}_t + \sigma_f \boldsymbol{\varepsilon}_{\mathbf{y},t}, \\ \mathbf{z}_{t+1} &= k_r \mathbf{z}_t - \alpha \mathbf{x}_t + \mathbf{b} + \sigma_r \boldsymbol{\varepsilon}_{\mathbf{z},t}, \end{cases} \quad (\text{S11})$$

where $\mathbf{W} = (w_{ij})_{N_{\text{node}} \times N_{\text{node}}}$, $\mathbf{x} = (x_1, x_2, \dots, x_{N_{\text{node}}})^\top$, $\mathbf{y} = (y_1, y_2, \dots, y_{N_{\text{node}}})^\top$, and $\mathbf{z} = (z_1, z_2, \dots, z_{N_{\text{node}}})^\top$.

In our simulation, we chose $N_{\text{node}} = 10$ and typical parameter values $s = 20$, $k_f = 0.2$, $k_r = 0.95$, and $b_i = 0.4$ for all i ; the coupling matrix $\mathbf{W} = (w_{ij})$ was constructed such that every neuron i received feedback inputs from two other neurons $j_1, j_2 \neq i$ with nonnegative couplings $w_{ij_1} + w_{ij_2} = 1$, where $(i, j), (w_{ij_1}, w_{ij_2})$ were generated randomly from uniform distributions; the coupling strengths and noise levels were $\alpha = 4$, $\beta = 0.2$ and $\sigma_f = \sigma_r = 0.05$, respectively. We generated 1000 time series \mathbf{x}_{obs} with data length 1000 after the relaxation time in 100 different networks (10 time series for each network). The values of IEE, GC, TE, and CCM were calculated from \mathbf{x}_{obs} solely. When calculating causal indices, we chose delayed lag $L = 3$, number of nearest neighbors $K = 40$. For the perturbed systems, we recorded the output $\mathbf{x}_{\text{per}}^{(i)}$ by removing neuron i (set as a constant zero). The Kullback-Leibler divergence (KLD) was used to measure the true influence of the perturbation between neurons, i.e.

$$D_{ij} \triangleq \text{KLD}[p_j(\mathbf{x}_{\text{obs}}) || p_j(\mathbf{x}_{\text{per}}^{(i)})] = \iint p_j(\mathbf{x}_{\text{obs}}) \log \frac{p_j(\mathbf{x}_{\text{obs}})}{p_j(\mathbf{x}_{\text{per}}^{(i)})} d\mathbf{x}_{\text{obs}} d\mathbf{x}_{\text{per}}^{(i)}, \quad (\text{S12})$$

where i and j are two different neurons, the perturbation is conducted on i , and $p_j(\mathbf{x}_{\text{obs}})$ and $p_j(\mathbf{x}_{\text{per}}^{(i)})$ represent the stationary probability density functions of j before and after the perturbation, respectively.

In Figs. 4(A-D) in the main text, the linear regression $y = ax + b$ was conducted on KLD and the four causal indices, i.e. IEE, GC, TE, and CCM. In Fig. 4(E) in the main text, we used the cosine similarity between KLD and the four causal indices. The cosine similarity between vectors \mathbf{A} and \mathbf{B} is defined as

$$S_C(\mathbf{A}, \mathbf{B}) = \frac{\mathbf{A} \cdot \mathbf{B}}{\|\mathbf{A}\| \|\mathbf{B}\|} = \frac{\sum_{i=1}^n A_i B_i}{\sqrt{\sum_{i=1}^n A_i^2} \cdot \sqrt{\sum_{i=1}^n B_i^2}}, \quad (\text{S13})$$

where A_i and B_i are the i th components of \mathbf{A} and \mathbf{B} , respectively.

2.7 *Caenorhabditis elegans* (*C. elegans*) neural activity dataset

We collected the calcium fluorescence imaging time series from neurons of a freely moving *C. elegans*, published in (1). *C. elegans* is a widely used model organism in neuroscience, and its nervous system connectomes, consisting of 302 neurons in the hermaphrodite, has been

comprehensively mapped (2). Due to the potential presence of strong synchrony among different neurons, inferring the causal network over the entire system can be challenging. Recently, Banerjee et al. (3) attempted synaptic connection inference on a symmetrically *folded* subnetwork composed of the most active motor neurons in the system. In our study, we carried out causality inference on a *reduced* network of neuron assemblies, formed by clustering neurons with highly similar activity.

2.7.1 Data Description

The experimental multi-neuron time series data of calcium imaging of *C. elegans* are obtained from (1), with a sampling rate of 2.13Hz and a temporal length of 18 min (i.e. 2300 samples). We focused on $N = 31$ neurons with specified functions (such as AVAL, AVAR, etc.). The 31 names of neurons can be found in table S5. We chose $T = 1750$ time points, during which the correlation pattern of the neural activity remains stable. Then, the following preprocessing procedures were conducted:

- *Detrending*: Considering the non-negative property of fluorescence intensity, the time series for each neuron is first shifted to have a zero minimum; then, each time series is dynamically normalized via dividing its 5-point moving average by its 401-point moving average. This transformation acts similarly to a band-pass filter, removing the trend in time series and stabilizing them.
- *Dimension reduction*: We normalized the time series to have unit second raw moments and denoted it as $\mathbf{X} = [\mathbf{x}_1, \mathbf{x}_2, \dots, \mathbf{x}_N] \in \mathbb{R}^{T \times N}$, where \mathbf{x}_i is the time series of neuron i . Let $\mathbf{S} = T^{-1} \mathbf{X}^\top \mathbf{X} = (s_{ij})$ be the cosine similarity matrix, where s_{ij} represents the cosine of the angle between time series from the i th and j th neurons. Apply eigen-decomposition on \mathbf{S} as $\mathbf{S} = \mathbf{Q}^\top \mathbf{\Lambda} \mathbf{Q}$, where \mathbf{Q} is an orthogonal matrix and $\mathbf{\Lambda}$ is a non-negative diagonal matrix. Thus, $\mathbf{P} = \mathbf{\Lambda}^{1/2} \mathbf{Q} = [\mathbf{p}_1, \mathbf{p}_2, \dots, \mathbf{p}_N]$ provides a dimension reduction of \mathbf{X} . The vector \mathbf{p}_i lies on the unit sphere in \mathbb{R}^N and $s_{ij} = \mathbf{p}_i^\top \mathbf{p}_j$, where $i, j = 1, 2, \dots, N$.
- *Clustering*: Then, we clustered the N neurons into M neuron assemblies, with sizes N_1, N_2, \dots, N_M , respectively. Denote $\mathbf{X}_m \in \mathbb{R}^{T \times N_m}$ and $\mathbf{S}_m \in \mathbb{R}^{N_m \times N_m}$ as the submatrices of \mathbf{X} and \mathbf{S} , which hold the time series data and similarity values within the m th assembly, respectively. The collective dynamics $\mathbf{Y} = [\mathbf{y}_1, \mathbf{y}_2, \dots, \mathbf{y}_M] \in \mathbb{R}^{T \times M}$ of each assembly in the reduced network is then represented by the dominant component of the PCA whitening of \mathbf{X}_m ; that is, given the eigen-decomposition $\mathbf{S}_m = \mathbf{Q}_m^\top \mathbf{\Lambda}_m \mathbf{Q}_m$ with $\mathbf{\Lambda}_m = \text{diag}\{\lambda_1(\mathbf{S}_m), \lambda_2(\mathbf{S}_m), \dots, \lambda_{N_m}(\mathbf{S}_m)\}$ in descending order, \mathbf{y}_m is the first column of $\mathbf{X}_m \mathbf{Q}_m^\top \mathbf{\Lambda}_m^{-1/2}$. The optimal clustering of neurons with similar dynamics is achieved by maximizing the fraction ρ of the energy that remains in the representing time series

\mathbf{Y} , where

$$\rho = \frac{1}{N} \sum_{m=1}^M \lambda_1(\mathbf{S}_m). \quad (\text{S14})$$

Practically, we found an approximate solution to the above problem simply by clustering points $\{\mathbf{p}_i\}$ using a k-means algorithm with the designated M , and then picked the result with the largest ρ from repeated trials of k-means clustering. In this study, $M = 7$ and $\rho_{\max} = 0.9514$ is the best result for clustering, and the clusters are listed in table S5. Most bilaterally symmetric neuron pairs have naturally fallen into the same assemblies, as designated in (3).

The original time series for each neuron are displayed in fig. S7(a), which is the same as Fig. 5(B) in the main text. fig. S7(b) is the Pearson correlation matrix of the time difference. The normalized time series \mathbf{X} are displayed in fig. S7(c). Figure S7(d) is the cosine similarity matrix \mathbf{S} , which is the same as Fig. 5(C) in the main text. The names of neurons in the same cluster are shown with the same color. The representative time series for individual neuron assemblies are shown in fig. S7(e) with the corresponding cosine similarity matrix shown in fig. S7(f).

2.7.2 Causality Analysis

Regarding to the ground truth of causalities between neurons, we referred to the quantitative connectomes of the adult hermaphrodite *C. elegans* described in Supplementary Information 5 of (2) and its further correction in (4). Both chemical and gap junction (electrical) synapses are provided. We denote the connection matrix for the reduced network as $\mathbf{C} = (c_{ij})_{M \times M}$. The value c_{ij} is simply obtained by merging the connectivity values from all neurons in the i th cluster to all those in the j th cluster. Since $M = 7$, we obtained a 7×7 directed network with 26 edges, whose elements range from 1 to 210.

For the inferred causal networks obtained from the neural activity data, we calculated four indices, i.e. IEE, GC (21), TE (22), and CCM (23), which are denoted as \mathbf{C}^{IEE} , \mathbf{C}^{GC} , \mathbf{C}^{TE} , and \mathbf{C}^{CCM} , respectively.

In our numerical experiments, each time series was decimated by a factor of 5 to obtain 5 time series, and the final causality strength was obtained by averaging the results from the 5 evaluations. Parameters were chosen as: delayed lag $L = 3$, number of nearest neighbors $K = 20$.

We demonstrated the ground truth causality strengths \mathbf{C} (in the logarithmic scale) in fig. S8(a), and the inferred causalities in figs. S8(b-e). We further compared the performance of different methods from two perspectives: binary classification and cosine similarity.

Binary classification. The ground truth \mathbf{C} has 26 causal edges (as “1”) and 16 non-causal edges (as “0”). We plotted the receiver operating characteristic (ROC) curves for \mathbf{C}^{IEE} , \mathbf{C}^{GC} , \mathbf{C}^{TE} , and \mathbf{C}^{CCM} in fig. S9, respectively. Four criteria were used to evaluate the performance of different algorithms:

- The area under the curve (AUC);
- Maximum Youden index, i.e. the maximum difference between the true positive rate and the false positive rate;
- Maximum concordance probability, i.e. the maximum product of sensitivity and specificity;
- Minimum distance to the point $(0, 1)$ for the ROC curve.

The last three indices are proposed for choosing the *optimal* operating point (OOP) on the ROC curve (24). Figure S9 marked the OOPs obtained by different criteria, and Table 2 in the main text listed the numerical values for four algorithms. We also plotted the true connectomes (Fig. 5(D) in the main text or fig. S10(a)) and inferred networks at the OOPs (Fig. 5(E) in the main text for IEE, fig. S10(b) for GC, fig. S10(c) for TE, fig. S10(d) for CCM) as graphs. At the minimum distance OOP points, IEE/GC/TE/CCM have the number of true positive edges as 22, 22, 21, 22, the false positive edges as 1, 2, 3, 4, the true negative edges as 15, 14, 13, 12, and the false negative edges as 4, 4, 5, 4, respectively (see table S6). IEE exhibited the best performance for binary classification in estimating neural connectomes of the *C. elegans*.

Cosine similarity. The cosine similarity values between the vectorized C and $C^{\text{IEE}}/C^{\text{GC}}/C^{\text{TE}}/C^{\text{CCM}}$ were calculated by Eq. (S13), respectively. Since c_{ij} ranges widely from 1 to 210, we also calculated the cosine similarity values between $\ln(1 + c_{ij})$ and the four inferred indices. As listed in Table 2 in the main text, in both cases c_{ij}^{IEE} shows the largest similarity to the ground truth, which indicates that IEE can effectively quantify the neural connectomes in *C. elegans*.

2.8 COVID-19 dataset

We explored the causal relationships in the inter-regional transmission of coronavirus (COVID-19) among the prefectures of Japan.

2.8.1 Time series data

The data on daily confirmed new COVID-19 cases in all 47 prefectures is available on the website of the Ministry of Health, Labour and Welfare of Japan (5). We collected data spanning a period of 1209 days from January 16, 2020 to May 8, 2023, as shown in Fig. S11(a). During this period, there were 8 waves of infection with the 9th beginning by the end of this period. The overall number of cases exhibited an exponentially increasing trend. We assume that COVID-19 spread across the country in a similar fashion, differing only in the scale from wave to wave. Additionally, a consistent variation pattern within the week is observable in the data. Therefore, the time series are preprocessed by dividing their 7-day moving averages by their 140-day moving averages to remove both the day-of-the-week variation and the trend.

2.8.2 Effective distance as the ground truth

We defined the concept of *effective distance* as the ground truth of causality between prefectures based on human mobility. In previous research, the geographical connections, specifically the geodesic distance, between metropolitan areas in Japan have been considered as the ground truth (25, 26). However, human mobility models can better reflect the social and economical connections between prefectures (27).

The definition of *effective distance* in this study is based on the *gravity model of human mobility*

$$F_{ij} = Km_i m_j f(d_{ij}), \quad (\text{S15})$$

where F_{ij} denotes the mobility flow from the i th community to the j th, the masses m_i and m_j describe the sizes of these communities, $f(d_{ij})$ represents a deterrence function which decreases with the distance d_{ij} between communities, and K is a constant (27, 28). Usually, the masses m_i and m_j can be various factors such as population, gdp-per-capita, etc. The distance d_{ij} can be measured in terms of geodesic distance, time, or monetary cost. Typically, a power or an exponential form is assumed for the deterrence function (27).

In this study, we collected *net* annual flows traveling between prefectures as the mobility data F_{ij} . The geodesic distance was used as d_{ij} . The proportion of the infectious population in prefecture i was denoted as ρ_i . The function $f(\cdot)$ was assumed to follow a power law. Denote

$$\mathcal{O}_i = \sum_{\substack{j=1 \\ j \neq i}}^{N_p} F_{ij}, \quad \mathcal{I}_j = \sum_{\substack{i=1 \\ i \neq j}}^{N_p} F_{ij}, \quad i, j = 1, 2, \dots, N_p, \quad (\text{S16})$$

where $N_p = 47$ is the number of prefectures, \mathcal{O}_i represents the total number of travelers leaving prefecture i , and \mathcal{I}_j is the total number of travelers arriving at prefecture j . According to Eq. (S15), for one person leaving prefecture i , the probability of his/her arrival at prefecture j is

$$P_{ij} := \frac{F_{ij}}{\mathcal{O}_i} \approx k_i \mathcal{I}_j d_{ij}^{\alpha_i}, \quad i, j = 1, 2, \dots, N_p, \quad i \neq j, \quad (\text{S17})$$

and for one person arriving at prefecture j , the probability of coming from prefecture i is

$$Q_{ij} := \frac{F_{ij}}{\mathcal{I}_j} \approx s_j \mathcal{O}_i d_{ij}^{\beta_j}, \quad i, j = 1, 2, \dots, N_p, \quad i \neq j, \quad (\text{S18})$$

where \mathcal{O}_i and \mathcal{I}_j are considered as the masses, while k_i and α_i are coefficients describing the willingness to travel of people in prefecture i , and s_j and β_j are coefficients describing the ability to attract tourists of prefecture j . These coefficients k_i , α_i , s_j and β_j were estimated by fitting from the data F_{ij} . We denote the estimated normalized transition probabilities as \hat{P} and \hat{Q} , where

$$\hat{P}_{ij} = \frac{k_i \mathcal{I}_j d_{ij}^{\alpha_i}}{\sum_{j=1}^{N_p} k_i \mathcal{I}_j d_{ij}^{\alpha_i}}, \quad \hat{Q}_{ij} = \frac{s_j \mathcal{O}_i d_{ij}^{\beta_j}}{\sum_{i=1}^{N_p} s_j \mathcal{O}_i d_{ij}^{\beta_j}}, \quad (\text{S19})$$

the row-sum of $\hat{P} \in \mathbb{R}^{N_p \times N_p}$ is 1, and the column-sum of $\hat{Q} \in \mathbb{R}^{N_p \times N_p}$ is 1.

Therefore, the number of infectious individuals T_{ij} traveling from prefecture i to j can be estimated using either $\rho_i \mathcal{O}_i \hat{P}_{ij}$ or $\rho_i \mathcal{I}_j \hat{Q}_{ij}$. We used their geometric mean value, i.e.

$$T_{ij} = \sqrt{\rho_i \mathcal{O}_i \hat{P}_{ij} \cdot \rho_i \mathcal{I}_j \hat{Q}_{ij}}, \quad (\text{S20})$$

where ρ_i is the infectious rate of COVID-19 in prefecture i . According to Eqs. (S17)-(S20), we can observe that T_{ij} follows a distribution $T_{ij} \sim d_{ij}^{(\alpha_i + \beta_j)/2}$. The *effective distance* is defined as

$$D_{ij}^{\text{COVID}} = T_{ij}^{2/(\alpha_i + \beta_j)} = (\rho_i^2 \mathcal{O}_i \mathcal{I}_j \hat{P}_{ij} \hat{Q}_{ij})^{\frac{2}{\alpha_i + \beta_j}} \quad (\text{S21})$$

to maintain the dimensionality $D_{ij}^{\text{COVID}} \sim d_{ij}$. Such an effective distance D_{ij}^{COVID} considers the effects of the geodesic distance, the human mobility, and the mass of communities. We used D_{ij}^{COVID} as the baseline reference for evaluating the performance of causality inference.

Data collection and preprocessing for estimating the effective distance:

- The *net* human mobility data F_{ij} among prefectures is available on the website of the Ministry of Land, Infrastructure, Transport and Tourism, as the result of the *Inter-Regional Travel Survey in Japan*, conducted every five years, most recently in 2015 (7). This survey counts the number of domestic passengers traveling across the borders of prefectures, using five inter-regional transportation modes including airlines, railways, sea lines, buses, and cars. There are missing values within travels among major metropolitan areas in Japan (i.e., Tokyo area including Tokyo, Kanagawa, Chiba, and Saitama; Kinki area including Osaka, Kyoto, Hyogo, and Nara; Chukyo area including Aichi, Gifu, and Mie). We filled by regression according to another survey named *Passenger Regional Flow Survey* conducted every year, which targets the *gross* annual passenger flow between prefectures (the corresponding 2015 data is available in (8)). The net flow considers the actual origin and destination of a passenger's trip, while the same trip gets separated by intermediate stops in the gross flow.
- The geodesic distances d_{ij} (measured between prefectural offices) are acquired from the website of the Geospatial Information Authority of Japan (6).
- Given F_{ij} and d_{ij} , the values of k_i , s_j , α_i and β_j are determined for all i and j by fitting according to Eq. (S17) and Eq. (S18). The exponents α_i and β_j range between -2.712 and -0.744 , with a median of -1.665 .
- The coefficient ρ_i , showing the proportion of infectious passengers, is defined as the ratio of the cumulative number of confirmed cases to the population in a prefecture. The cumulative number is calculated from the daily confirmed new cases from (5), while the population were collected from the counts by Japanese government in October 1st, 2021 (9).

The net human mobility flows F_{ij} , the geodesic distances d_{ij} , and the effective distances D_{ij}^{COVID} are demonstrated in figs. S11(b), (c), and (d), respectively. From fig. S11(c), we observe that metropolitan areas with small geodesic distances appear as clusters of prefectures. Meanwhile, after considering the effect of human mobility, population sizes, and infectious rate, we obtained the effective distance matrix in fig. S11(d), in which strips of relatively small effective distances connect those metropolitan areas and other prefectures.

2.8.3 Causality Analysis

We computed the causality strengths between any two nodes in the network (i.e., prefectures in Japan) with IEE/GC/TE/CCM. Each time series is divided into 3 segments of equal lengths (keeping the sample rate) in order to achieve multiple evaluations of the indices. All segments were normalized to have zero mean and unit variance. To avoid zero values, a Gaussian noise with mean zero and standard variation 10^{-7} was added to the time series. Parameters in the algorithm were chosen as: delayed lag $L = 3$, number of nearest neighbors $K = 20$.

IEE demonstrated highly linear correlation with $\ln D^{\text{COVID}}$ with PCC -0.906 from Tokyo ($i = 13$) to other other prefectures (Fig. 6(A) in the main text). Further, in Fig. 6(B) in the main text and fig. S12, we exhibit five other prefectures including Osaka, Aichi, Hokkaido, Fukuoka, and Okinawa, where IEE showed linearity with $\ln D^{\text{COVID}}$. Figure S13 plots the causality strengths c_{ij}^{Inf} given by IEE/GC/TE/CCM with respect to the effective distance D_{ij}^{COVID} from Tokyo ($i = 13$) to other other prefectures ($j \neq i$). Table 3 in the main text lists an overall comparison, and IEE has an average PCC 0.748 with the logarithm of D^{COVID} , higher than GC (0.166), TE (0.109), and CCM (0.585). In this example, the CCM index was transformed by $-\log(1 - x)$ to scale its value from 0 to $+\infty$, ensuring a consistent range as D^{COVID} for comparison purposes. These results indicate that the proposed criterion c^{IEE} is suitable for the quantitative analyses of the causality in the COVID-19 transmission dynamics in Japan.

2.9 Circadian rhythm gene expression dataset

We investigated the gene regulatory networks (GRNs) involving key genes related to circadian rhythm. The gene expression time series that were measured by Affimetrix microarray (Genechip Rat Genome 230 2.0) of the laboratory rat (*Rattus norvegicus*) cultured cells sampled from suprachiasmatic nucleus (SCN) for studying circadian rhythm (10, 11, 29–31). We downloaded the dataset from <https://github.com/Partial-Cross-Mapping/circadian>, which contained the ground truth of GRN in the gene and protein level and four time series (with length 9, 16, 14, and 12) for gene expressions. After interpolating and concatenating, we obtained 98 time points for causal detection.

Through decades of molecular and genetic studies (32, 33), lots of key circadian genes have been identified and extensively studied in mammals, including *Bmal1*(*Arntl*), *Clock*, *Cry1*, *Cry2*, *Dec1*(*Bhlhb2*), *Dec2*(*Bhlhb3*), *Per1*, *Per2*, *Per3*. We focused on two subnetworks at the protein-protein interaction level in our experiment. One is surrounding *Clock*, which is com-

prised by 12 genes (Fig. 6(D) in the main text). The transcription factor *Clock* is phosphorylated by PFK family genes. The other network containing 14 genes is centered around *Cry1/Cry2*, phosphorylated by MAPK family genes (fig. S14(a)).

We thus applied IEE/GC/TE/CCM to the time-series data to detect the causal relationship between genes. The ROC curves and AUC values were computed and displayed in Fig. 6(E) for the *Clock* network and fig. S14(b) for the *Cry1/Cry2* network. IEE designed for quantifying the IntDC performed higher AUC values than the other three ObsDC indices. Parameters in algorithm were chosen as: delayed lag $L = 3$, number of nearest neighbors $K = 20$.

2.10 Conditional interventional embedding entropy

In the main text, we describe the IEE criterion for a two-variable dynamical system. To distinguish directed and indirect causality, we can generalize the system consisting of multiple variables. For simplicity, the dynamics of y can be considered as

$$y_{t+1} = f(x_t, \dots, x_{t-p}, y_t, \dots, y_{t-p}, z_t, \dots, z_{t-p}, \varepsilon_{y,t}), \quad (\text{S22})$$

and the embedding theorem ensures that

$$\mathbf{X}_t = \mathbf{F}(\mathbf{Y}_{t+1}, \mathbf{Z}_t), \quad (\text{S23})$$

where z_t is a third variable whose time-delay vector is \mathbf{Z}_t . Under an infinitesimal intervention, we can obtain

$$\delta \mathbf{X}_t = \nabla \mathbf{F}(\mathbf{Y}_{t+1}, \mathbf{Z}_t) \cdot (\delta \mathbf{Y}_{t+1}, \delta \mathbf{Z}_t). \quad (\text{S24})$$

Thus, the IEE can be extended to its conditional version

$$\text{cIEE}[x \rightarrow y|z] = \text{CMI}(\delta \mathbf{X}_t, \delta \mathbf{Y}_{t+1} | \mathbf{Y}_{t+1}, \mathbf{Z}_t, \delta \mathbf{Z}_t), \quad (\text{S25})$$

where “cIEE” is short for conditional IEE.

3 Supplementary Figures

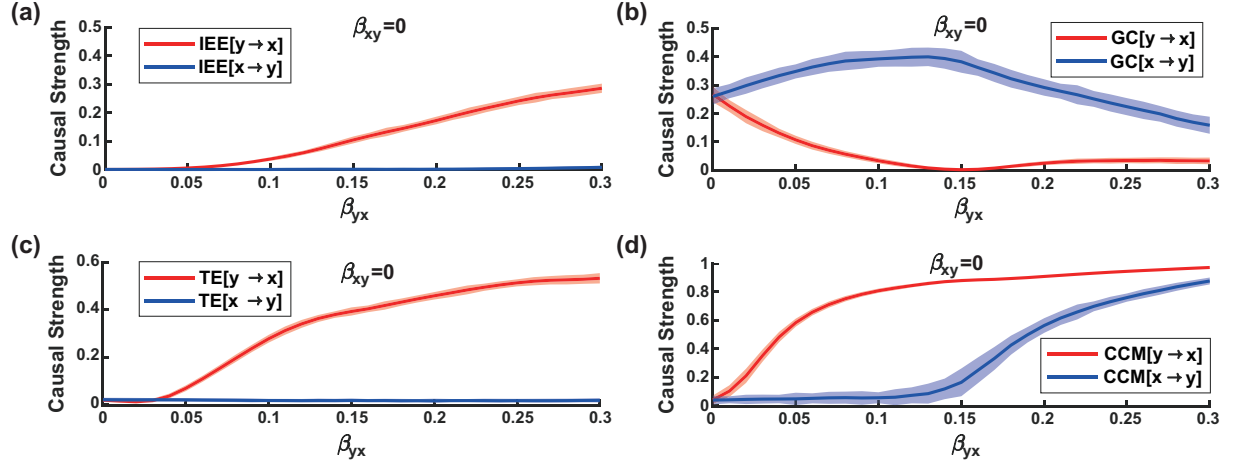


Figure S1: Comparison of (a) IEE, (b) GC, (c) TE, and (d) CCM on the two-node Logistic system ($\beta_{xy} = 0$). The parameter β_{yx} increases from 0 to 0.3. GC is non-monotonic. $TE[y \rightarrow x]$ slightly decreases around 0.025 and being smaller than $TE[x \rightarrow y]$, which induces the false negative problem. CCM has the false positive problem for $x \rightarrow y$, especially when $\beta_{yx} > 0.15$.

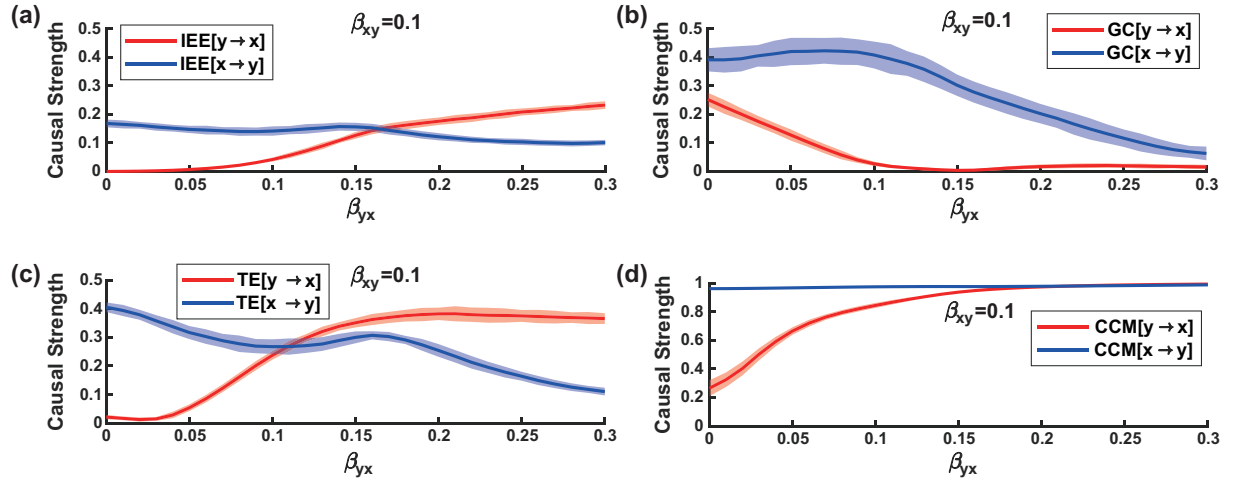


Figure S2: Comparison of (a) IEE, (b) GC, (c) TE, and (d) CCM on the two-node Logistic system ($\beta_{xy} = 0.1$). The parameter β_{yx} increases from 0 to 0.3. GC is non-monotonic. $TE[y \rightarrow x]$ slightly decreases around 0.025 and after 0.2. $CCM[y \rightarrow x]$ has the false positive problem even when $\beta_{yx} = 0$.

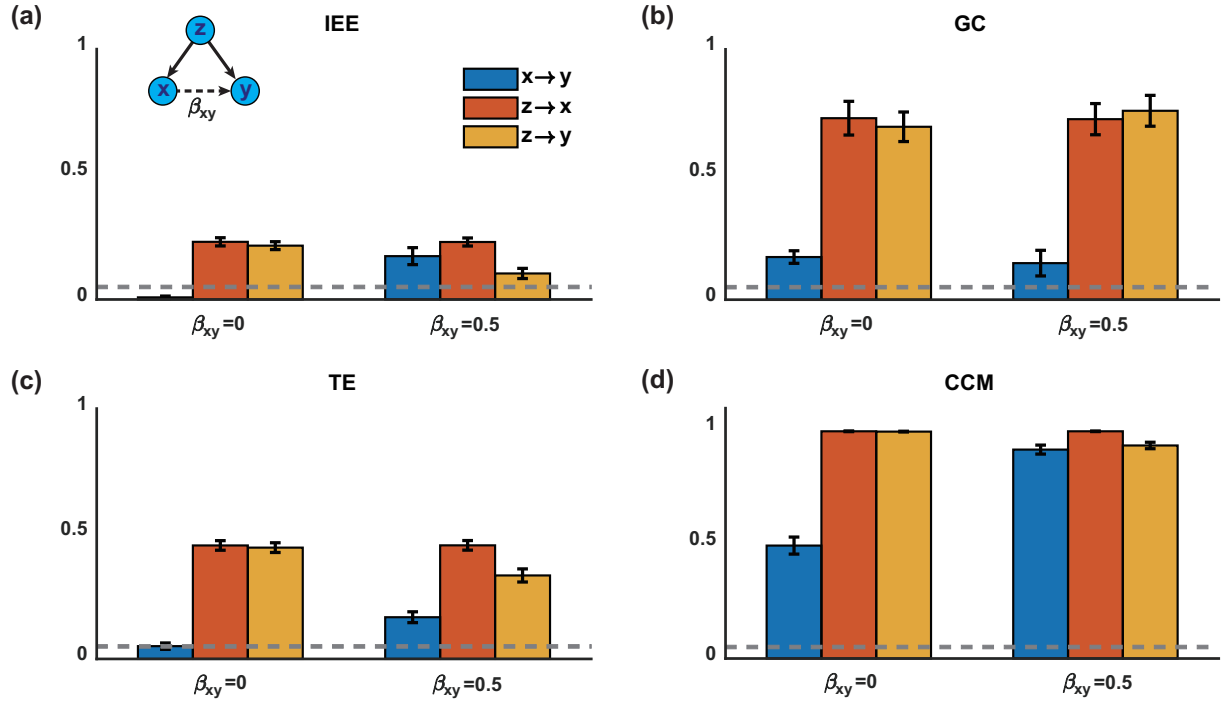


Figure S3: Comparison of (a) IEE, (b) GC, (c) TE, and (d) CCM on the three-node Logistic system. There are constant causal effects from z to x and from z to y . The variable z acts as a confounder. When $\beta_{xy} = 0$ there is no causality from x to y , while causality exists from x to y when $\beta_{xy} = 0.5$. The gray dashed line represents 0.05 for reference. IEE for IntDC accurately distinguish the causal strength between x and y , while the other three indices for ObsDC suffer from false-positive detections when a confounding variable z exists.

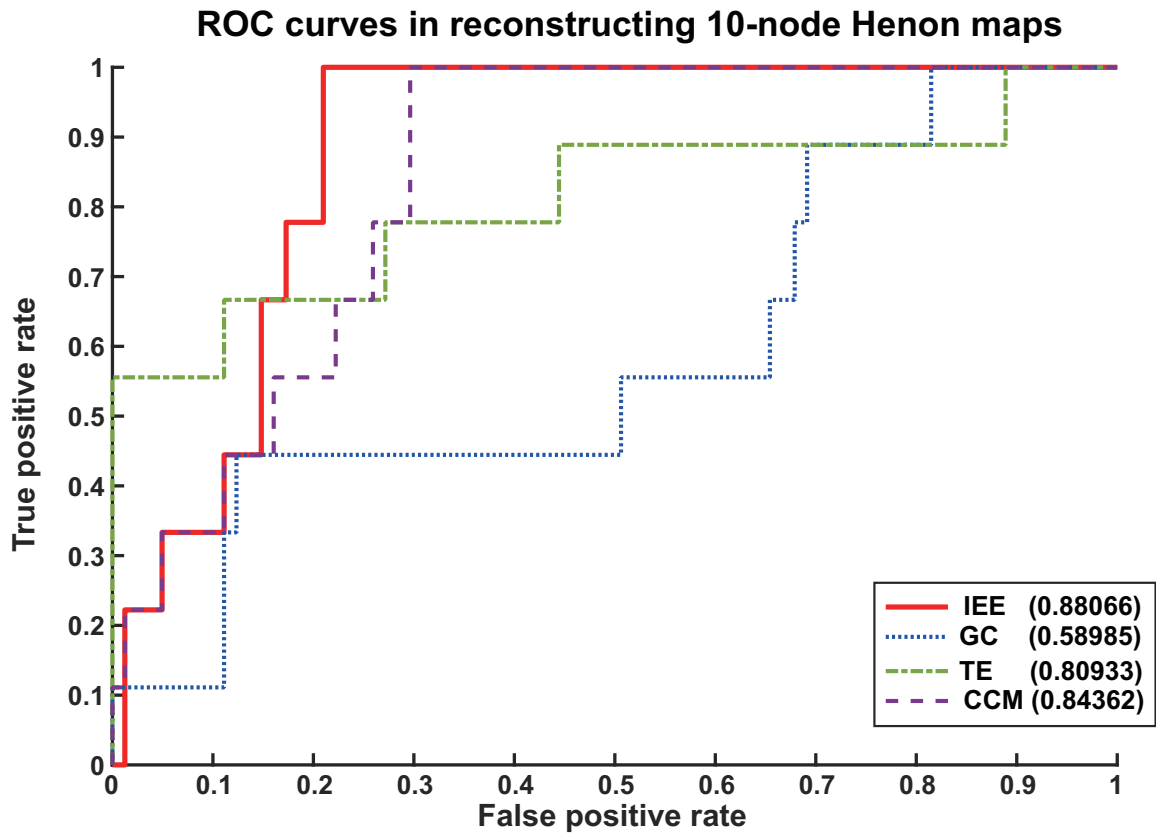


Figure S4: The ROC curves for IEE, GC, TE, and CCM when reconstructing the 10-node Honon maps in a representative simulation. The values in the legend are AUC values for the corresponding ROC curves.

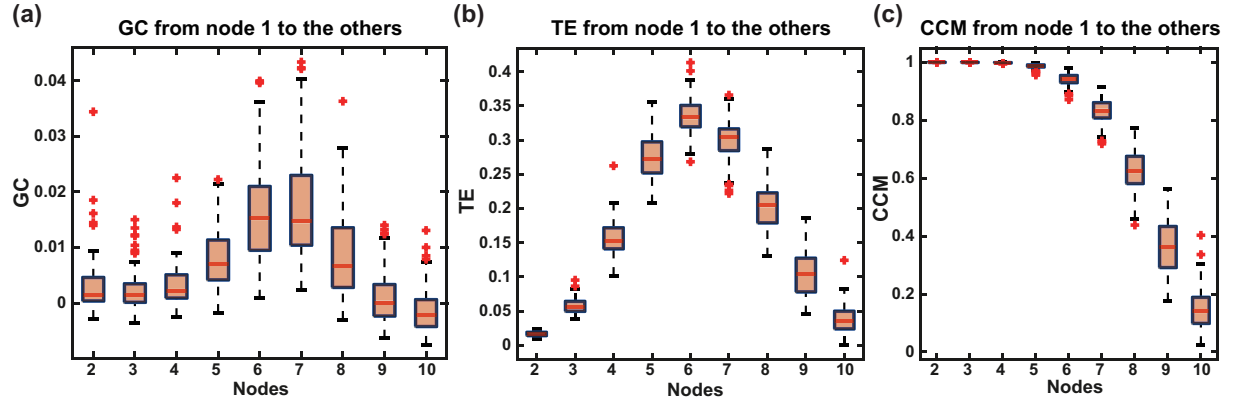


Figure S5: GC, TE, and CCM from the Node 1 to the other nine nodes in the 10-node coupled Henon-map network. GC and TE are not monotonically decreasing. CCM presents strong causalities from Node 1 to the Nodes 2-6.

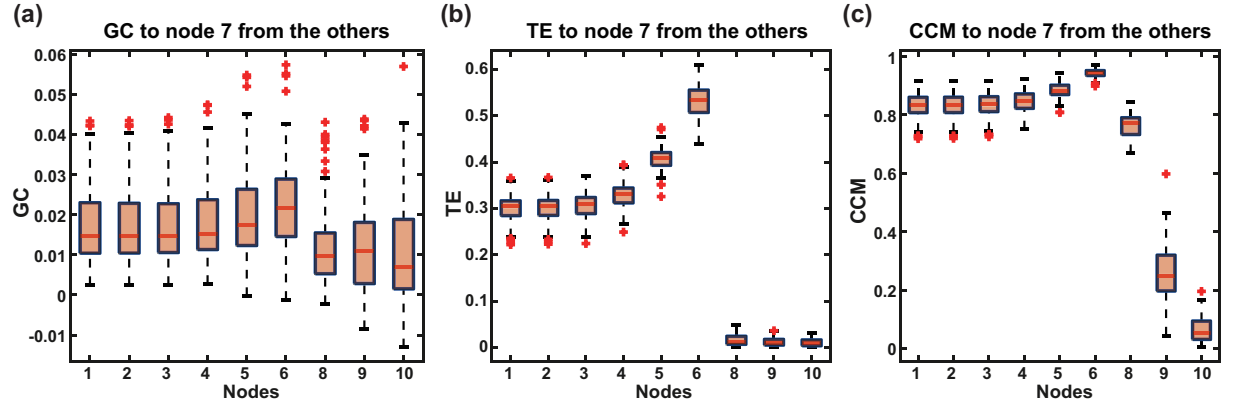


Figure S6: GC, TE, and CCM to the Node 7 from the other nine nodes in the 10-node coupled Henon-map network. GC fails the causal detection, while CCM has a false positive result from Node 8 to Node 7.

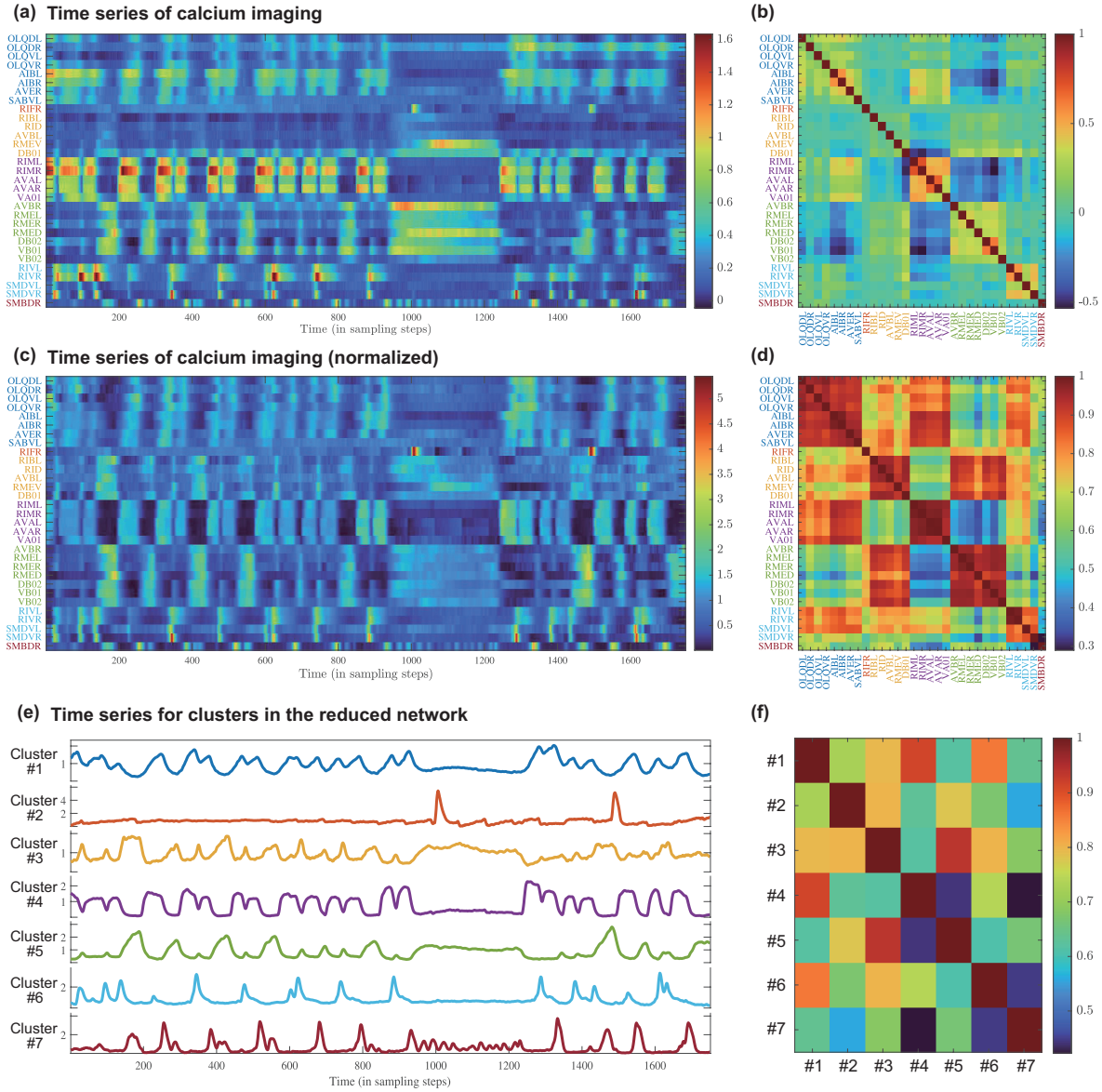


Figure S7: Data in the analysis of calcium imaging of a freely moving *C. elegans* worm. (a) Time series for 31 individual neurons as published in Ref. (1). (b) Pearson correlation matrix for the time difference of the time series shown in (a). (c) Time series after preprocessing. (d) Cosine similarity matrix for the time series shown in (c). In (a-d), the neurons belonging to the same cluster are grouped and their names are color-coded accordingly. (e) Representative time series illustrating the collective behavior of each neuron cluster. (f) Similarity matrix for the time series shown in (e).

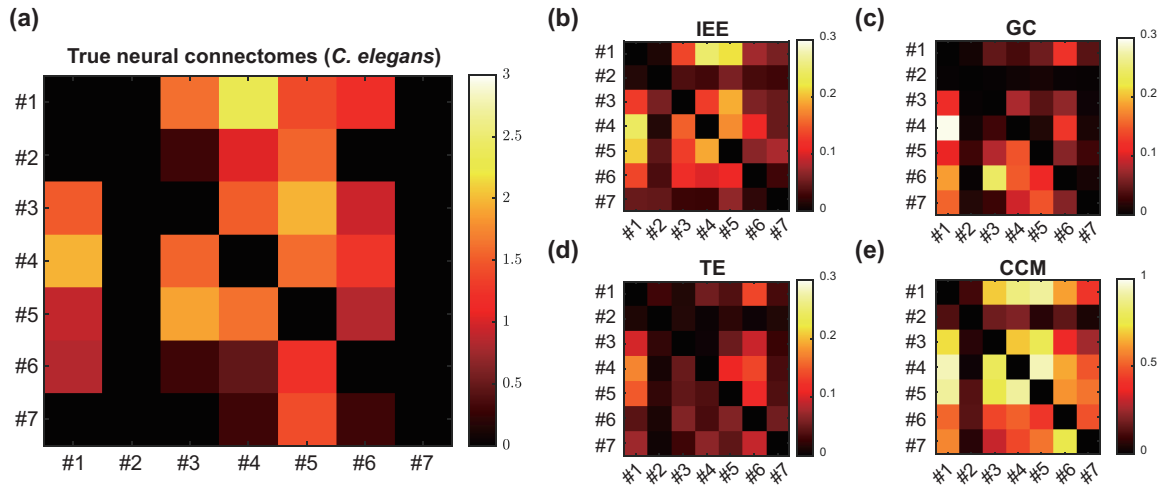


Figure S8: Heat maps of connection strengths between neural clusters in *C. elegans*. (a) Ground truth connectomes C (in a logarithmic scale, i.e. $\log(1 + C)$). (b-e) Inferred causality strengths by IEE/GC/TE/CCM, denoted as $C^{\text{IEE}}/C^{\text{GC}}/C^{\text{TE}}/C^{\text{CCM}}$, respectively.

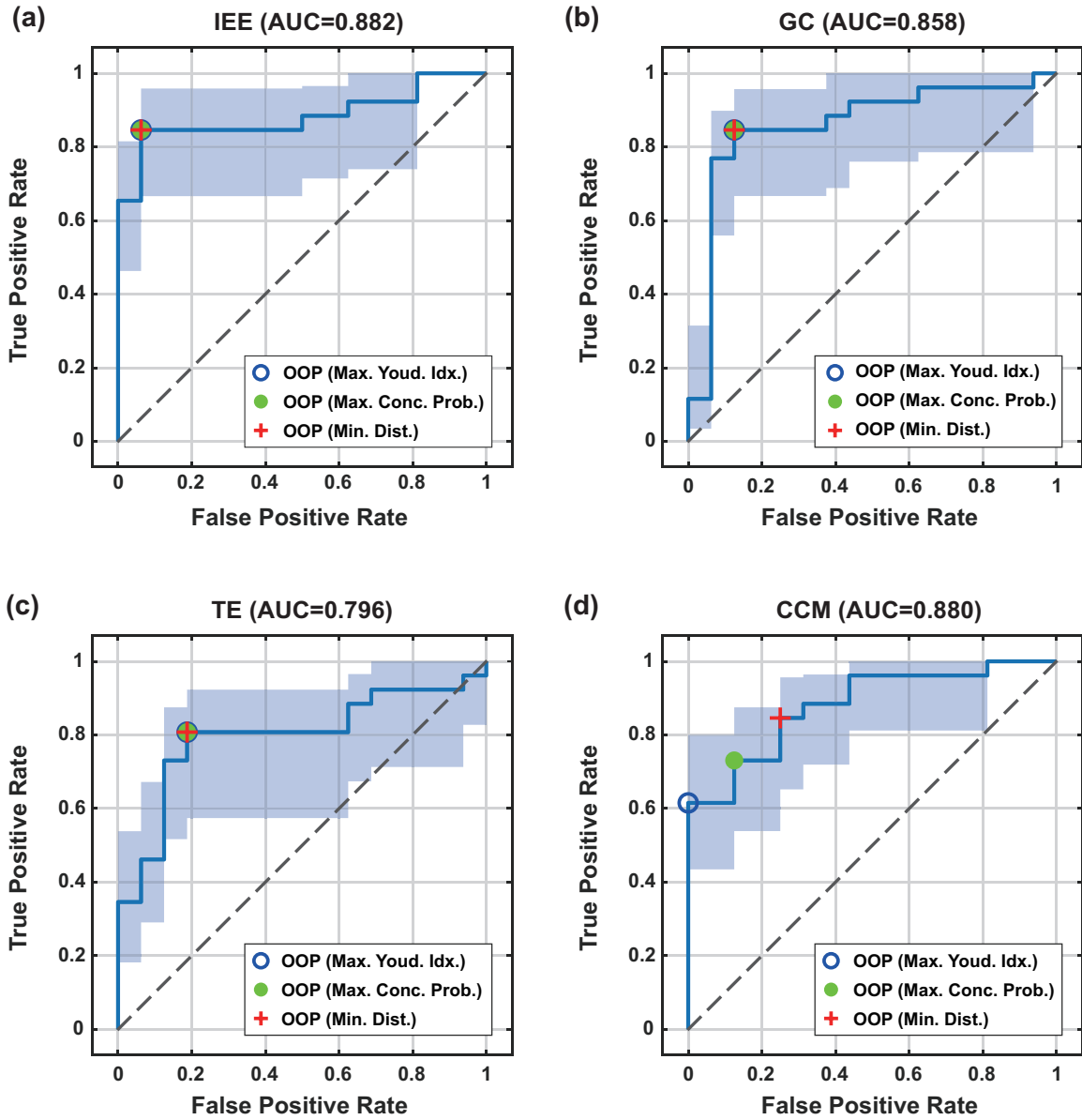


Figure S9: Receiver operating characteristic (ROC) curves in the inference of *C. elegans* neural connectomes by (a) IEE, (b) GC, (c) TE, and (d) CCM. Optimal operating points (OOPs) obtained by the maximum Youden index (blue circles), the maximum concordance probability (green dots), and the minimum distance to the point (0, 1) (red crosses) are marked. AUC values are listed. The shaded area around the ROC curve represents the 95% confidence interval obtained by bootstrapping.

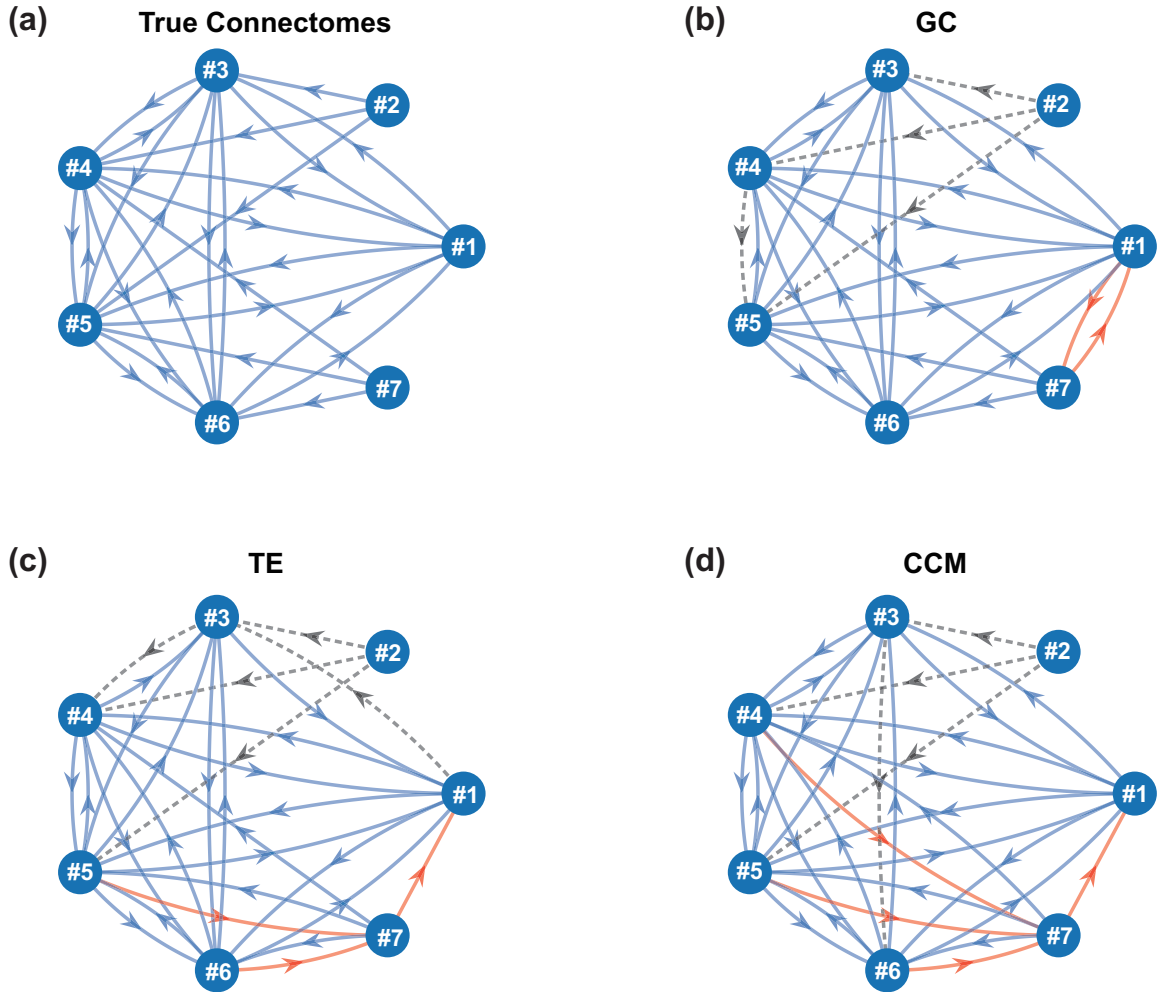


Figure S10: (a) The true neural connectomes between the seven clusters in *C. elegans*. (b-d) The inferred causal networks by GC/TE/CCM at the optimal operating points given by the minimum distance index. The red edges represent false positives, and the black dashed edges are false negatives.

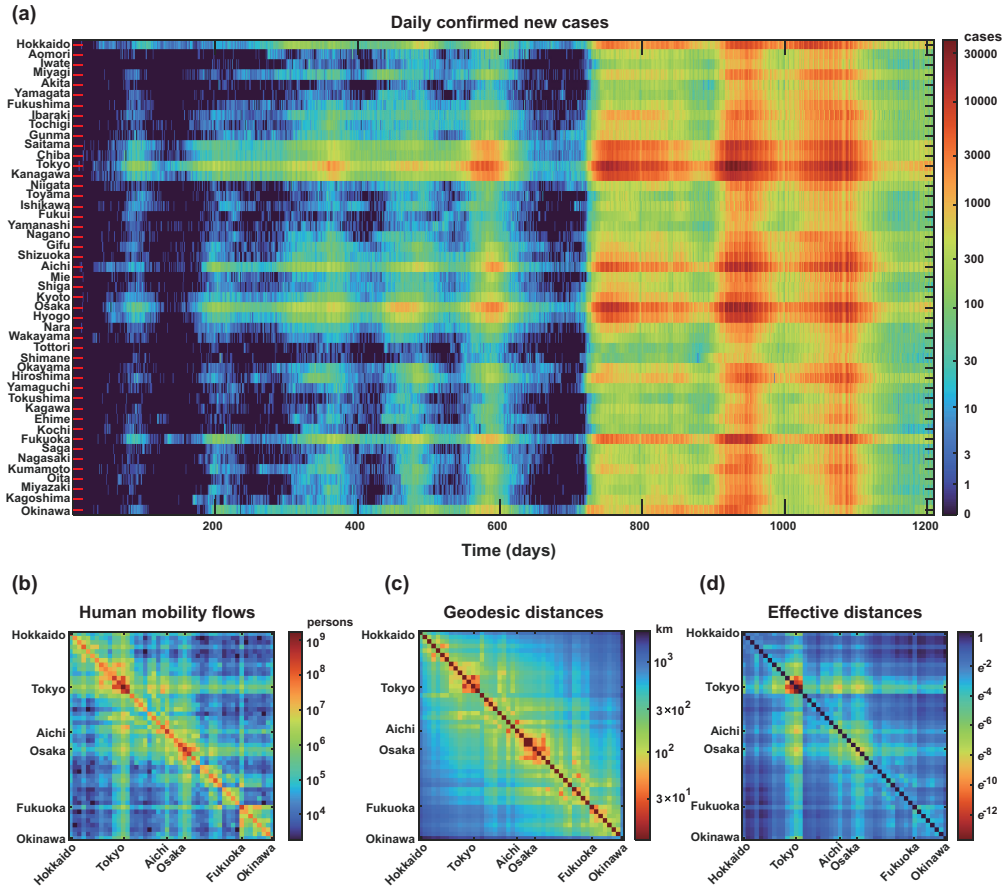


Figure S11: Data involved in the analysis of COVID-19 transmission in Japan. (a) The time series of daily confirmed new cases in each prefecture, showing 8 waves of infection from January 16, 2020 to May 8, 2023 (1209 days). (b) The net human mobility flows F_{ij} (after completing missing values). (c) The geodesic distances d_{ij} (in kilometers) between prefectures. (d) The effective distances D_{ij}^{COVID} defined by Eq. (S21) (shown in a logarithmic scale). D_{ij}^{COVID} was used as a baseline reference for the causal inference.

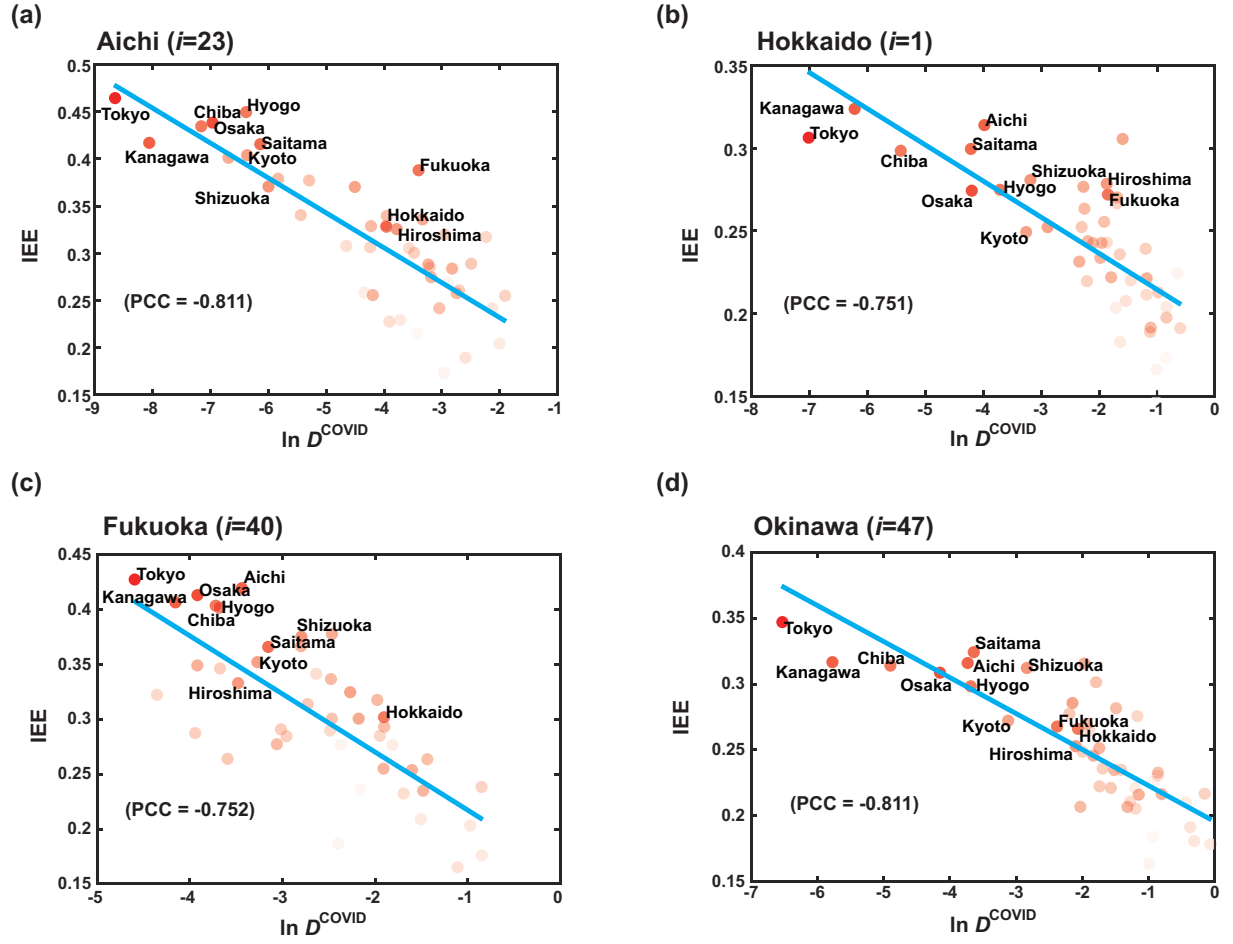


Figure S12: Scatter plots of the inferred causal strengths IEE with respect to the logarithmic of effective distances D_{ij}^{COVID} , from Aichi/Hokkaido/Fukuoka/Okinawa to other prefectures. The color depth of dots represents the number of confirmed COVID-19 cases in the corresponding prefecture. The blue line is the least square line. Pearson correlation coefficient (PCC) is shown, and IEE can reflect the influence of disease transmission.

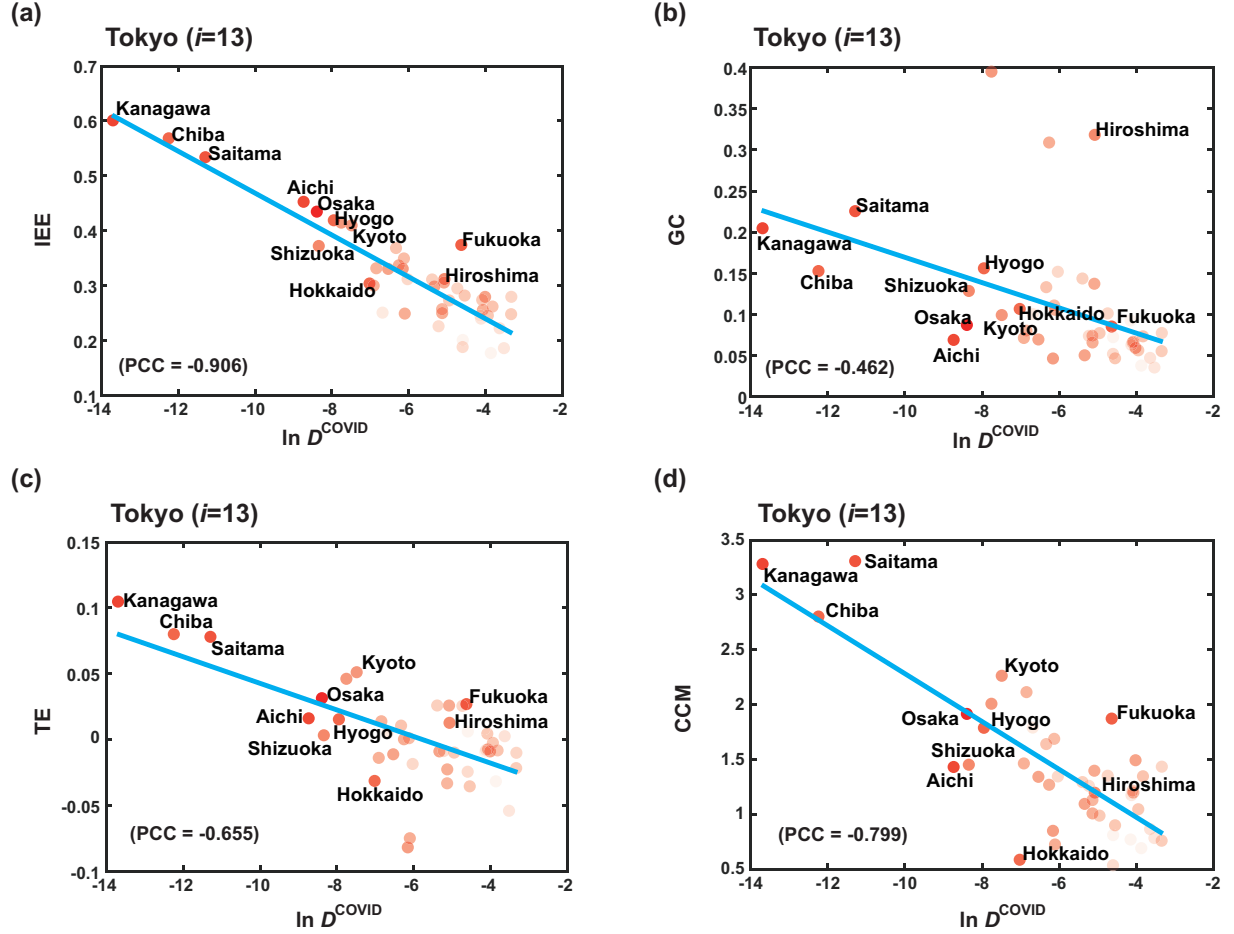


Figure S13: Scatter plots of the inferred causal strengths IEE/GC/TE/CCM with respect to the logarithmic of effective distances, i.e. $\ln D_{ij}^{\text{COVID}}$, from Tokyo ($i = 13$) to other prefectures. The CCM index was transformed by $-\log(1 - x)$ to scale its value from 0 to $+\infty$, ensuring a consistent range as D^{COVID} for comparison purposes. The color depth of dots represents the number of confirmed COVID-19 cases in the corresponding prefecture. The blue line is the least square line. Pearson correlation coefficient (PCC) is shown, and IEE is the best to reflect the influence of disease transmission.

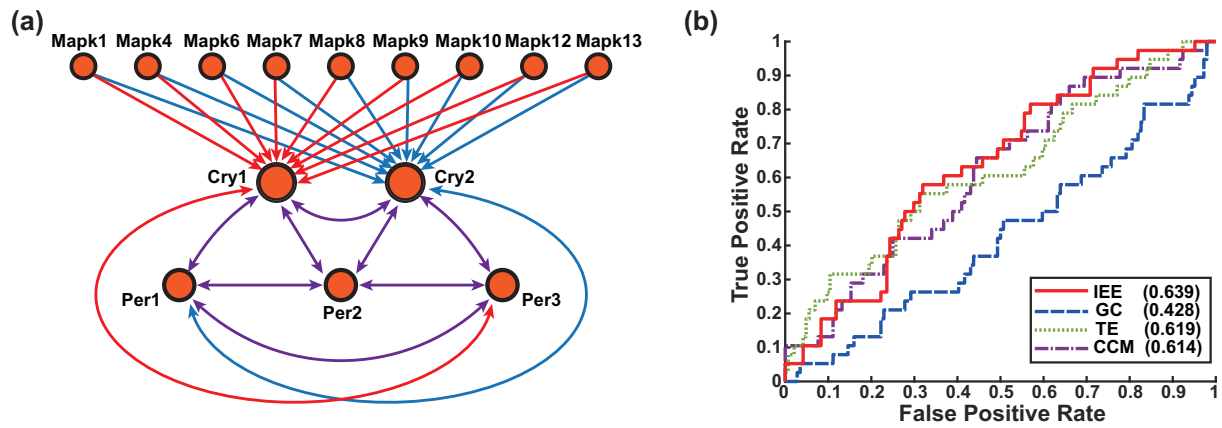


Figure S14: Comparison results for detecting causality in the gene regulatory network (GRN) centered around *Cry1* and *Cry2*. (a) The ground truth of the GRN surrounding *Cry1* and *Cry2*. There are 14 genes in total. Key circadian genes *Cry1*, *Cry2*, *Per1*, *Per2*, and *Per3* are highlighted by large node sizes. Distinct colors are employed to differentiate crossing arrows. (b) The ROC curves of IEE (red solid line), GC (blue dashed line), TE (green dotted line), and CCM (purple dash-dot line). The AUC values for each method are listed in the legend.

4 Supplementary Tables

Table S1: The mean values (standard variations) of four causal indices from y to x when $\beta_{xy} = 0$ in fig. S1.

When $\beta_{yx} = 0$, $\text{IEE}[y \rightarrow x] = 9.42e - 05$ ($9.16e - 04$), $\text{GC}[y \rightarrow x] = 2.67e - 01$ ($2.75e - 02$), $\text{TE}[y \rightarrow x] = 2.01e - 02$ ($7.54e - 03$), $\text{CCM}[y \rightarrow x] = 4.21e - 02$ ($3.04e - 02$)					
β_{yx}	0.01	0.02	0.03	0.04	0.05
$\text{IEE}[y \rightarrow x]$	$1.07e - 04$ ($1.06e - 03$)	$3.66e - 04$ ($1.22e - 03$)	$9.56e - 04$ ($1.51e - 03$)	$2.59e - 03$ ($2.17e - 03$)	$4.75e - 03$ ($2.52e - 03$)
$\text{GC}[y \rightarrow x]$	$2.22e - 01$ ($2.09e - 02$)	$1.89e - 01$ ($2.32e - 02$)	$1.56e - 01$ ($2.09e - 02$)	$1.31e - 01$ ($1.54e - 02$)	$1.06e - 01$ ($1.44e - 02$)
$\text{TE}[y \rightarrow x]$	$1.77e - 02$ ($7.58e - 03$)	$1.02e - 02$ ($6.38e - 03$)	$1.04e - 02$ ($7.77e - 03$)	$3.39e - 02$ ($1.01e - 02$)	$6.71e - 02$ ($1.20e - 02$)
$\text{CCM}[y \rightarrow x]$	$6.79e - 02$ ($4.09e - 02$)	$2.02e - 01$ ($4.98e - 02$)	$3.63e - 01$ ($4.25e - 02$)	$4.95e - 01$ ($3.60e - 02$)	$5.93e - 01$ ($2.81e - 02$)
β_{yx}	0.06	0.07	0.08	0.09	0.10
$\text{IEE}[y \rightarrow x]$	$7.86e - 03$ ($2.96e - 03$)	$1.24e - 02$ ($3.98e - 03$)	$1.91e - 02$ ($4.72e - 03$)	$2.67e - 02$ ($5.69e - 03$)	$3.69e - 02$ ($6.33e - 03$)
$\text{GC}[y \rightarrow x]$	$8.50e - 02$ ($1.38e - 02$)	$7.00e - 02$ ($1.23e - 02$)	$5.77e - 02$ ($1.08e - 02$)	$4.34e - 02$ ($1.02e - 02$)	$3.44e - 02$ ($9.11e - 03$)
$\text{TE}[y \rightarrow x]$	$1.09e - 01$ ($1.27e - 02$)	$1.52e - 01$ ($1.37e - 02$)	$1.95e - 01$ ($1.54e - 02$)	$2.40e - 01$ ($1.53e - 02$)	$2.80e - 01$ ($1.63e - 02$)
$\text{CCM}[y \rightarrow x]$	$6.64e - 01$ ($2.32e - 02$)	$7.16e - 01$ ($2.13e - 02$)	$7.54e - 01$ ($1.87e - 02$)	$7.88e - 01$ ($1.62e - 02$)	$8.10e - 01$ ($1.50e - 02$)
β_{yx}	0.11	0.12	0.13	0.14	0.15
$\text{IEE}[y \rightarrow x]$	$4.69e - 02$ ($8.07e - 03$)	$5.78e - 02$ ($7.42e - 03$)	$7.23e - 02$ ($9.30e - 03$)	$8.93e - 02$ ($1.06e - 02$)	$1.04e - 01$ ($1.20e - 02$)
$\text{GC}[y \rightarrow x]$	$2.37e - 02$ ($8.51e - 03$)	$1.44e - 02$ ($7.11e - 03$)	$8.24e - 03$ ($4.96e - 03$)	$3.21e - 03$ ($2.75e - 03$)	$1.67e - 03$ ($1.73e - 03$)
$\text{TE}[y \rightarrow x]$	$3.16e - 01$ ($1.74e - 02$)	$3.43e - 01$ ($1.66e - 02$)	$3.65e - 01$ ($1.47e - 02$)	$3.84e - 01$ ($1.37e - 02$)	$3.93e - 01$ ($1.72e - 02$)
$\text{CCM}[y \rightarrow x]$	$8.28e - 01$ ($1.48e - 02$)	$8.45e - 01$ ($1.22e - 02$)	$8.60e - 01$ ($1.21e - 02$)	$8.74e - 01$ ($1.07e - 02$)	$8.82e - 01$ ($1.14e - 02$)
β_{yx}	0.16	0.17	0.18	0.19	0.20
$\text{IEE}[y \rightarrow x]$	$1.19e - 01$ ($1.16e - 02$)	$1.32e - 01$ ($1.47e - 02$)	$1.45e - 01$ ($1.18e - 02$)	$1.56e - 01$ ($1.19e - 02$)	$1.72e - 01$ ($1.33e - 02$)
$\text{GC}[y \rightarrow x]$	$2.31e - 03$ ($1.64e - 03$)	$7.33e - 03$ ($3.81e - 03$)	$(1.45e - 02$ ($5.67e - 03$))	$2.08e - 02$ ($7.10e - 03$)	$2.48e - 02$ ($6.92e - 03$)
$\text{TE}[y \rightarrow x]$	$4.04e - 01$ ($1.41e - 02$)	$4.17e - 01$ ($1.76e - 02$)	$4.34e - 01$ ($1.52e - 02$)	$4.47e - 01$ ($1.49e - 02$)	$4.59e - 01$ ($1.56e - 02$)
$\text{CCM}[y \rightarrow x]$	$8.84e - 01$ ($9.86e - 03$)	$8.89e - 01$ ($1.02e - 02$)	$8.93e - 01$ ($9.71e - 03$)	$9.02e - 01$ ($8.59e - 03$)	$9.09e - 01$ ($9.67e - 03$)
β_{yx}	0.21	0.22	0.23	0.24	0.25
$\text{IEE}[y \rightarrow x]$	$1.88e - 01$ ($1.31e - 02$)	$2.02e - 01$ ($1.59e - 02$)	$2.16e - 01$ ($1.44e - 02$)	$2.29e - 01$ ($1.44e - 02$)	$2.40e - 01$ ($1.46e - 02$)
$\text{GC}[y \rightarrow x]$	$3.05e - 02$ ($7.91e - 03$)	$3.27e - 02$ ($9.32e - 03$)	$3.33e - 02$ ($8.70e - 03$)	$3.44e - 02$ ($1.01e - 02$)	$3.44e - 02$ ($9.38e - 03$)
$\text{TE}[y \rightarrow x]$	$4.73e - 01$ ($1.76e - 02$)	$4.84e - 01$ ($1.86e - 02$)	$4.97e - 01$ ($1.51e - 02$)	$5.06e - 01$ ($1.50e - 02$)	$5.14e - 01$ ($1.49e - 02$)
$\text{CCM}[y \rightarrow x]$	$9.17e - 01$ ($8.29e - 03$)	$9.25e - 01$ ($8.79e - 03$)	$9.32e - 01$ ($7.10e - 03$)	$9.39e - 01$ ($6.87e - 03$)	$9.46e - 01$ ($6.60e - 03$)
β_{yx}	0.26	0.27	0.28	0.29	0.30
$\text{IEE}[y \rightarrow x]$	$2.55e - 01$ ($1.70e - 02$)	$2.62e - 01$ ($1.42e - 02$)	$2.68e - 01$ ($1.58e - 02$)	$2.77e - 01$ ($1.61e - 02$)	$2.85e - 01$ ($1.63e - 02$)
$\text{GC}[y \rightarrow x]$	$3.57e - 02$ ($1.03e - 02$)	$3.44e - 02$ ($1.04e - 02$)	$3.61e - 02$ ($1.16e - 02$)	$3.20e - 02$ ($1.09e - 02$)	$3.33e - 02$ ($1.18e - 02$)
$\text{TE}[y \rightarrow x]$	$5.23e - 01$ ($1.73e - 02$)	$5.27e - 01$ ($1.77e - 02$)	$5.26e - 01$ ($1.94e - 02$)	$5.29e - 01$ ($1.93e - 02$)	$5.34e - 01$ ($2.18e - 02$)
$\text{CCM}[y \rightarrow x]$	$9.50e - 01$ ($6.87e - 03$)	$9.56e - 01$ ($7.11e - 03$)	$9.61e - 01$ ($6.17e - 03$)	$9.68e - 01$ ($5.61e - 03$)	$9.72e - 01$ ($5.54e - 03$)

Table S2: The mean values (standard variations) of four causal indices from x to y when $\beta_{xy} = 0$ in fig. S1.

When $\beta_{yx} = 0$, $\text{IEE}[x \rightarrow y] = 1.50e - 04$ ($8.61e - 04$), $\text{GC}[x \rightarrow y] = 2.60e - 01$ ($2.90e - 02$), $\text{TE}[x \rightarrow y] = 2.20e - 02$ ($7.80e - 03$), $\text{CCM}[x \rightarrow y] = 4.10e - 02$ ($3.03e - 02$)					
β_{yx}	0.01	0.02	0.03	0.04	0.05
IEE[$x \rightarrow y$]	$1.34e - 04$ ($9.62e - 04$)	$2.23e - 05$ ($1.17e - 03$)	$2.25e - 04$ ($1.43e - 03$)	$1.97e - 04$ ($1.52e - 03$)	$3.48e - 04$ ($1.89e - 03$)
GC[$x \rightarrow y$]	$2.78e - 01$ ($2.49e - 02$)	$2.98e - 01$ ($2.89e - 02$)	$3.18e - 01$ ($2.75e - 02$)	$3.32e - 01$ ($2.79e - 02$)	$3.49e - 01$ ($2.47e - 02$)
TE[$x \rightarrow y$]	$2.18e - 02$ ($8.20e - 03$)	$2.03e - 02$ ($8.05e - 03$)	$2.13e - 02$ ($7.30e - 03$)	$2.24e - 02$ ($7.57e - 03$)	$2.01e - 02$ ($7.55e - 03$)
CCM[$x \rightarrow y$]	$4.19e - 02$ ($2.47e - 02$)	$4.54e - 02$ ($3.27e - 02$)	$4.93e - 02$ ($3.15e - 02$)	$4.81e - 02$ ($2.98e - 02$)	$4.74e - 02$ ($4.32e - 02$)
β_{yx}	0.06	0.07	0.08	0.09	0.10
IEE[$x \rightarrow y$]	$5.70e - 05$ ($2.36e - 03$)	$2.18e - 05$ ($2.19e - 03$)	$9.17e - 05$ ($2.61e - 03$)	$3.04e - 04$ ($2.64e - 03$)	$1.30e - 04$ ($3.37e - 03$)
GC[$x \rightarrow y$]	$3.63e - 01$ ($2.83e - 02$)	$3.78e - 01$ ($2.85e - 02$)	$3.84e - 01$ ($3.26e - 02$)	$3.92e - 01$ ($3.11e - 02$)	$3.89e - 01$ ($2.78e - 02$)
TE[$x \rightarrow y$]	$2.03e - 02$ ($7.32e - 03$)	$2.04e - 02$ ($7.72e - 03$)	$1.85e - 02$ ($7.78e - 03$)	$1.89e - 02$ ($8.19e - 03$)	$1.81e - 02$ ($6.66e - 03$)
CCM[$x \rightarrow y$]	$5.23e - 02$ ($3.54e - 02$)	$5.91e - 02$ ($4.22e - 02$)	$5.82e - 02$ ($4.24e - 02$)	$5.64e - 02$ ($4.77e - 02$)	$5.25e - 02$ ($3.86e - 02$)
β_{yx}	0.11	0.12	0.13	0.14	0.15
IEE[$x \rightarrow y$]	$2.44e - 04$ ($3.40e - 03$)	$1.07e - 03$ ($3.52e - 03$)	$4.58e - 04$ ($3.42e - 03$)	$9.51e - 04$ ($3.72e - 03$)	$9.80e - 04$ ($3.42e - 03$)
GC[$x \rightarrow y$]	$4.00e - 01$ ($2.99e - 02$)	$4.00e - 01$ ($3.32e - 02$)	$4.00e - 01$ ($3.25e - 02$)	$4.00e - 01$ ($3.58e - 02$)	$3.82e - 01$ ($3.85e - 02$)
TE[$x \rightarrow y$]	$1.77e - 02$ ($6.98e - 03$)	$1.84e - 02$ ($7.07e - 03$)	$1.70e - 02$ ($7.89e - 03$)	$1.93e - 02$ ($7.57e - 03$)	$1.76e - 02$ ($7.63e - 03$)
CCM[$x \rightarrow y$]	$6.24e - 02$ ($5.62e - 02$)	$6.75e - 02$ ($5.63e - 02$)	$9.20e - 02$ ($7.02e - 02$)	$9.88e - 02$ ($7.22e - 02$)	$1.68e - 01$ ($9.74e - 02$)
β_{yx}	0.16	0.17	0.18	0.19	0.20
IEE[$x \rightarrow y$]	$6.97e - 05$ ($2.44e - 03$)	$1.08e - 03$ ($2.68e - 03$)	$2.12e - 04$ ($2.82e - 03$)	$1.02e - 03$ ($3.26e - 03$)	$7.20e - 02$ ($2.77e - 03$)
GC[$x \rightarrow y$]	$3.64e - 01$ ($2.92e - 02$)	$3.38e - 01$ ($3.17e - 02$)	$3.25e - 01$ ($3.12e - 02$)	$3.04e - 01$ ($2.91e - 02$)	$2.91e - 01$ ($2.89e - 02$)
TE[$x \rightarrow y$]	$1.89e - 02$ ($6.83e - 03$)	$1.69e - 02$ ($7.40e - 03$)	$1.85e - 02$ ($7.63e - 03$)	$1.68e - 02$ ($6.88e - 03$)	$1.72e - 02$ ($8.70e - 03$)
CCM[$x \rightarrow y$]	$2.29e - 01$ ($9.05e - 02$)	$3.52e - 01$ ($8.07e - 02$)	$4.19e - 01$ ($6.69e - 02$)	$5.08e - 01$ ($5.44e - 02$)	$5.71e - 01$ ($5.15e - 02$)
β_{yx}	0.21	0.22	0.23	0.24	0.25
IEE[$x \rightarrow y$]	$1.17e - 03$ ($3.00e - 03$)	$1.30e - 03$ ($3.26e - 03$)	$2.22e - 03$ ($4.05e - 03$)	$2.82e - 03$ ($4.09e - 03$)	$2.89e - 03$ ($4.70e - 03$)
GC[$x \rightarrow y$]	$2.80e - 01$ ($2.65e - 02$)	$2.64e - 01$ ($3.34e - 02$)	$2.54e - 01$ ($2.78e - 02$)	$2.36e - 01$ ($3.01e - 02$)	$2.22e - 01$ ($3.01e - 02$)
TE[$x \rightarrow y$]	$1.77e - 02$ ($6.70e - 03$)	$1.86e - 02$ ($6.57e - 03$)	$1.74e - 02$ ($7.94e - 03$)	$1.76e - 02$ ($8.16e - 03$)	$1.73e - 02$ ($7.51e - 03$)
CCM[$x \rightarrow y$]	$6.14e - 01$ ($4.87e - 02$)	$6.67e - 01$ ($5.24e - 02$)	$6.98e - 01$ ($3.47e - 02$)	$7.33e - 01$ ($3.46e - 02$)	$7.64e - 01$ ($2.88e - 02$)
β_{yx}	0.26	0.27	0.28	0.29	0.30
IEE[$x \rightarrow y$]	$3.60e - 03$ ($4.18e - 03$)	$4.79e - 03$ ($4.48e - 03$)	$5.39e - 03$ ($5.48e - 03$)	$6.40e - 03$ ($5.13e - 03$)	$7.48e - 03$ ($5.27e - 03$)
GC[$x \rightarrow y$]	$2.14e - 01$ ($3.05e - 02$)	$1.97e - 01$ ($2.76e - 02$)	$1.85e - 01$ ($2.83e - 02$)	$1.64e - 01$ ($2.77e - 02$)	$1.59e - 01$ ($2.99e - 02$)
TE[$x \rightarrow y$]	$1.84e - 02$ ($8.08e - 03$)	$1.69e - 02$ ($8.32e - 03$)	$1.75e - 02$ ($8.22e - 03$)	$1.92e - 02$ ($8.06e - 03$)	$1.89e - 02$ ($8.76e - 03$)
CCM[$x \rightarrow y$]	$7.85e - 01$ ($3.18e - 02$)	$8.14e - 01$ ($3.03e - 02$)	$8.35e - 01$ ($2.81e - 02$)	$8.60e - 01$ ($2.55e - 02$)	$8.77e - 01$ ($2.42e - 02$)

Table S3: The mean values (standard variations) of four causal indices from y to x when $\beta_{xy} = 0.1$ in fig. S2.

When $\beta_{yx} = 0$, $\text{IEE}[y \rightarrow x] = 2.24e - 04$ ($1.68e - 03$), $\text{GC}[y \rightarrow x] = 2.52e - 01$ ($2.38e - 02$), $\text{TE}[y \rightarrow x] = 2.10e - 02$ ($7.35e - 03$), $\text{CCM}[y \rightarrow x] = 2.64e - 01$ ($5.55e - 02$)					
β_{yx}	0.01	0.02	0.03	0.04	0.05
IEE[$y \rightarrow x$]	$1.16e - 04$ ($1.67e - 03$)	$7.81e - 04$ ($1.82e - 03$)	$1.79e - 03$ ($2.01e - 03$)	$3.68e - 03$ ($2.66e - 03$)	$6.24e - 03$ ($2.71e - 03$)
GC[$y \rightarrow x$]	$2.27e - 01$ ($2.43e - 02$)	$1.98e - 01$ ($2.07e - 02$)	$1.77e - 01$ ($1.93e - 02$)	$1.52e - 01$ ($1.85e - 02$)	$1.26e - 01$ ($1.96e - 02$)
TE[$y \rightarrow x$]	$1.81e - 02$ ($6.47e - 03$)	$1.03e - 02$ ($7.21e - 03$)	$8.56e - 03$ ($6.59e - 03$)	$2.48e - 02$ ($1.14e - 02$)	$5.14e - 02$ ($1.17e - 02$)
CCM[$y \rightarrow x$]	$3.01e - 01$ ($5.10e - 02$)	$4.05e - 01$ ($4.83e - 02$)	$5.03e - 01$ ($4.24e - 02$)	$6.01e - 01$ ($3.33e - 02$)	$6.71e - 01$ ($2.61e - 02$)
β_{yx}	0.06	0.07	0.08	0.09	0.10
IEE[$y \rightarrow x$]	$1.00e - 02$ ($4.00e - 03$)	$1.44e - 02$ ($3.86e - 03$)	$2.11e - 02$ ($4.88e - 03$)	$2.94e - 02$ ($5.09e - 03$)	$4.19e - 02$ ($6.86e - 03$)
GC[$y \rightarrow x$]	$1.04e - 01$ ($1.69e - 02$)	$7.90e - 02$ ($1.63e - 02$)	$5.68e - 02$ ($1.56e - 02$)	$3.88e - 02$ ($1.02e - 02$)	$2.40e - 02$ ($7.48e - 03$)
TE[$y \rightarrow x$]	$8.45e - 02$ ($1.31e - 02$)	$1.20e - 01$ ($1.35e - 02$)	$1.61e - 01$ ($1.47e - 02$)	$2.03e - 01$ ($1.59e - 02$)	$2.40e - 01$ ($1.52e - 02$)
CCM[$y \rightarrow x$]	$7.23e - 01$ ($2.39e - 02$)	$7.66e - 01$ ($1.91e - 02$)	$7.98e - 01$ ($1.81e - 02$)	$8.20e - 01$ ($1.83e - 02$)	$8.45e - 01$ ($1.75e - 02$)
β_{yx}	0.11	0.12	0.13	0.14	0.15
IEE[$y \rightarrow x$]	$5.41e - 02$ ($9.36e - 03$)	$7.19e - 02$ ($9.84e - 03$)	$8.93e - 02$ ($1.15e - 02$)	$1.07e - 01$ ($8.68e - 03$)	$1.28e - 01$ ($1.16e - 02$)
GC[$y \rightarrow x$]	$1.71e - 02$ ($6.09e - 03$)	$1.16e - 02$ ($3.32e - 03$)	$9.26e - 03$ ($5.65e - 03$)	$5.30e - 03$ ($3.76e - 03$)	$2.13e - 03$ ($2.33e - 03$)
TE[$y \rightarrow x$]	$2.70e - 01$ ($1.86e - 02$)	$3.00e - 01$ ($1.34e - 02$)	$3.22e - 01$ ($1.70e - 02$)	$3.40e - 01$ ($1.46e - 02$)	$3.54e - 01$ ($1.65e - 02$)
CCM[$y \rightarrow x$]	$8.67e - 01$ ($1.57e - 02$)	$8.87e - 01$ ($1.29e - 02$)	$9.06e - 01$ ($9.28e - 03$)	$9.23e - 01$ ($9.13e - 03$)	$9.39e - 01$ ($7.44e - 03$)
β_{yx}	0.16	0.17	0.18	0.19	0.20
IEE[$y \rightarrow x$]	$1.44e - 01$ ($1.26e - 02$)	$1.56e - 01$ ($1.39e - 02$)	$1.62e - 01$ ($1.42e - 02$)	$1.68e - 01$ ($1.39e - 02$)	$1.78e - 01$ ($1.31e - 02$)
GC[$y \rightarrow x$]	$3.23e - 03$ ($3.56e - 03$)	$7.42e - 03$ ($5.14e - 03$)	$1.20e - 02$ ($6.38e - 03$)	$1.48e - 02$ ($6.59e - 03$)	$1.66e - 02$ ($7.31e - 03$)
TE[$y \rightarrow x$]	$3.60e - 01$ ($1.94e - 02$)	$3.74e - 01$ ($1.94e - 02$)	$3.76e - 01$ ($2.05e - 02$)	$3.79e - 01$ ($2.34e - 02$)	$3.86e - 01$ ($2.17e - 02$)
CCM[$y \rightarrow x$]	$9.49e - 01$ ($6.94e - 03$)	$9.57e - 01$ ($5.78e - 03$)	$9.64e - 01$ ($4.15e - 03$)	$9.70e - 01$ ($3.69e - 03$)	$9.74e - 01$ ($3.43e - 03$)
β_{yx}	0.21	0.22	0.23	0.24	0.25
IEE[$y \rightarrow x$]	$1.82e - 01$ ($1.47e - 02$)	$1.89e - 01$ ($1.46e - 02$)	$1.93e - 01$ ($1.30e - 02$)	$2.03e - 01$ ($1.50e - 02$)	$2.09e - 01$ ($1.23e - 02$)
GC[$y \rightarrow x$]	$1.89e - 02$ ($7.54e - 03$)	$1.86e - 02$ ($7.85e - 03$)	$2.09e - 02$ ($8.17e - 03$)	$2.05e - 02$ ($7.67e - 03$)	$2.01e - 02$ ($6.96e - 03$)
TE[$y \rightarrow x$]	$3.83e - 01$ ($2.65e - 02$)	$3.80e - 01$ ($2.52e - 02$)	$3.76e - 01$ ($2.62e - 02$)	$3.77e - 01$ ($2.47e - 02$)	$3.78e - 01$ ($2.08e - 02$)
CCM[$y \rightarrow x$]	$9.78e - 01$ ($2.89e - 03$)	$9.81e - 01$ ($2.42e - 03$)	$9.84e - 01$ ($1.97e - 03$)	$9.86e - 01$ ($1.77e - 03$)	$9.87e - 01$ ($1.57e - 03$)
β_{yx}	0.26	0.27	0.28	0.29	0.30
IEE[$y \rightarrow x$]	$2.13e - 01$ ($1.25e - 02$)	$2.15e - 01$ ($1.29e - 02$)	$2.25e - 01$ ($1.05e - 02$)	$2.25e - 01$ ($1.39e - 02$)	$2.32e - 01$ ($1.34e - 02$)
GC[$y \rightarrow x$]	$1.82e - 02$ ($8.20e - 03$)	$1.84e - 02$ ($7.83e - 03$)	$1.65e - 02$ ($6.42e - 03$)	$1.72e - 02$ ($7.68e - 03$)	$1.56e - 02$ ($7.53e - 03$)
TE[$y \rightarrow x$]	$3.71e - 01$ ($2.33e - 02$)	$3.71e - 01$ ($2.23e - 02$)	$3.72e - 01$ ($1.86e - 02$)	$3.66e - 01$ ($2.11e - 02$)	$3.66e - 01$ ($1.88e - 02$)
CCM[$y \rightarrow x$]	$9.89e - 01$ ($1.34e - 03$)	$9.90e - 01$ ($1.08e - 03$)	$9.92e - 01$ ($8.64e - 04$)	$9.93e - 01$ ($8.94e - 04$)	$9.93e - 01$ ($7.65e - 04$)

Table S4: The mean values (standard variations) of four causal indices from x to y when $\beta_{xy} = 0.1$ in fig. S2.

When $\beta_{yx} = 0$, $\text{IEE}[x \rightarrow y] = 1.68e - 01$ ($1.35e - 02$), $\text{GC}[x \rightarrow y] = 3.91e - 01$ ($4.07e - 02$), $\text{TE}[x \rightarrow y] = 4.06e - 01$ ($1.67e - 02$), $\text{CCM}[x \rightarrow y] = 9.61e - 01$ ($3.05e - 03$)					
β_{yx}	0.01	0.02	0.03	0.04	0.05
IEE[$x \rightarrow y$]	$1.67e - 01$ ($1.41e - 02$)	$1.59e - 01$ ($1.17e - 02$)	$1.58e - 01$ ($1.31e - 02$)	$1.49e - 01$ ($1.18e - 02$)	$1.46e - 01$ ($1.26e - 02$)
GC[$x \rightarrow y$]	$3.85e - 01$ ($4.48e - 02$)	$3.97e - 01$ ($4.46e - 02$)	$4.02e - 01$ ($3.77e - 02$)	$4.15e - 01$ ($4.60e - 02$)	$4.19e - 01$ ($4.78e - 02$)
TE[$x \rightarrow y$]	$3.99e - 01$ ($1.96e - 02$)	$3.79e - 01$ ($1.75e - 02$)	$3.61e - 01$ ($1.99e - 02$)	$3.35e - 01$ ($2.36e - 02$)	$3.17e - 01$ ($2.28e - 02$)
CCM[$x \rightarrow y$]	$9.62e - 01$ ($2.96e - 03$)	$9.62e - 01$ ($3.00e - 03$)	$9.64e - 01$ ($3.16e - 03$)	$9.66e - 01$ ($3.00e - 03$)	$9.67e - 01$ ($2.84e - 03$)
β_{yx}	0.06	0.07	0.08	0.09	0.10
IEE[$x \rightarrow y$]	$1.45e - 01$ ($1.52e - 02$)	$1.42e - 01$ ($1.29e - 02$)	$1.39e - 01$ ($1.52e - 02$)	$1.38e - 01$ ($1.41e - 02$)	$1.42e - 01$ ($1.64e - 02$)
GC[$x \rightarrow y$]	$4.26e - 01$ ($4.72e - 02$)	$4.17e - 01$ ($4.51e - 02$)	$4.24e - 01$ ($4.77e - 02$)	$4.22e - 01$ ($4.50e - 02$)	$4.08e - 01$ ($4.70e - 02$)
TE[$x \rightarrow y$]	$2.99e - 01$ ($2.55e - 02$)	$2.92e - 01$ ($2.40e - 02$)	$2.74e - 01$ ($2.89e - 02$)	$2.67e - 01$ ($2.49e - 02$)	$2.67e - 01$ ($2.57e - 02$)
CCM[$x \rightarrow y$]	$9.69e - 01$ ($2.65e - 03$)	$9.70e - 01$ ($2.34e - 03$)	$9.71e - 01$ ($2.61e - 03$)	$9.73e - 01$ ($2.37e - 03$)	$9.75e - 01$ ($2.44e - 03$)
β_{yx}	0.11	0.12	0.13	0.14	0.15
IEE[$x \rightarrow y$]	$1.45e - 01$ ($1.44e - 02$)	$1.47e - 01$ ($1.69e - 02$)	$1.54e - 01$ ($1.51e - 02$)	$1.56e - 01$ ($1.43e - 02$)	$1.61e - 01$ ($1.43e - 02$)
GC[$x \rightarrow y$]	$3.94e - 01$ ($5.21e - 02$)	$3.79e - 01$ ($4.33e - 02$)	$3.61e - 01$ ($4.47e - 02$)	$3.34e - 01$ ($4.14e - 02$)	$2.99e - 01$ ($3.75e - 02$)
TE[$x \rightarrow y$]	$2.69e - 01$ ($2.85e - 02$)	$2.68e - 01$ ($2.56e - 02$)	$2.77e - 01$ ($2.42e - 02$)	$2.86e - 01$ ($2.32e - 02$)	$3.04e - 01$ ($2.07e - 02$)
CCM[$x \rightarrow y$]	$9.75e - 01$ ($2.19e - 03$)	$9.76e - 01$ ($2.25e - 03$)	$9.76e - 01$ ($2.02e - 03$)	$9.77e - 01$ ($1.96e - 03$)	$9.76e - 01$ ($2.07e - 03$)
β_{yx}	0.16	0.17	0.18	0.19	0.20
IEE[$x \rightarrow y$]	$1.51e - 01$ ($1.38e - 02$)	$1.46e - 01$ ($1.45e - 02$)	$1.34e - 01$ ($1.26e - 02$)	$1.28e - 01$ ($1.30e - 02$)	$1.21e - 01$ ($1.27e - 02$)
GC[$x \rightarrow y$]	$2.72e - 01$ ($3.70e - 02$)	$2.62e - 01$ ($3.69e - 02$)	$2.39e - 01$ ($3.76e - 02$)	$2.16e - 01$ ($3.67e - 02$)	$2.06e - 01$ ($3.41e - 02$)
TE[$x \rightarrow y$]	$3.10e - 01$ ($1.43e - 02$)	$3.08e - 01$ ($1.62e - 02$)	$2.91e - 01$ ($1.44e - 02$)	$2.75e - 01$ ($2.05e - 02$)	$2.56e - 01$ ($2.23e - 02$)
CCM[$x \rightarrow y$]	$9.75e - 01$ ($1.87e - 03$)	$9.76e - 01$ ($1.77e - 03$)	$9.77e - 01$ ($1.77e - 03$)	$9.77e - 01$ ($2.07e - 03$)	$9.78e - 01$ ($1.70e - 03$)
β_{yx}	0.21	0.22	0.23	0.24	0.25
IEE[$x \rightarrow y$]	$1.15e - 01$ ($1.12e - 02$)	$1.12e - 01$ ($1.08e - 02$)	$1.06e - 01$ ($9.21e - 03$)	$1.06e - 01$ ($1.08e - 02$)	$1.02e - 01$ ($1.09e - 02$)
GC[$x \rightarrow y$]	$1.86e - 01$ ($3.37e - 02$)	$1.66e - 01$ ($3.74e - 02$)	$1.47e - 01$ ($3.73e - 02$)	$1.32e - 01$ ($3.32e - 02$)	$1.17e - 01$ ($3.06e - 02$)
TE[$x \rightarrow y$]	$2.32e - 01$ ($2.18e - 02$)	$2.13e - 01$ ($2.20e - 02$)	$1.93e - 01$ ($1.96e - 02$)	$1.79e - 01$ ($1.89e - 02$)	$1.64e - 01$ ($1.56e - 02$)
CCM[$x \rightarrow y$]	$9.79e - 01$ ($1.59e - 03$)	$9.80e - 01$ ($1.45e - 03$)	$9.81e - 01$ ($1.47e - 03$)	$9.82e - 01$ ($1.57e - 03$)	$9.83e - 01$ ($1.52e - 03$)
β_{yx}	0.26	0.27	0.28	0.29	0.30
IEE[$x \rightarrow y$]	$1.02e - 01$ ($1.01e - 02$)	$9.79e - 02$ ($1.00e - 02$)	$9.85e - 02$ ($1.04e - 02$)	$9.74e - 02$ ($9.77e - 03$)	$1.01e - 01$ ($9.39e - 03$)
GC[$x \rightarrow y$]	$1.01e - 01$ ($3.14e - 02$)	$8.70e - 02$ ($2.79e - 02$)	$7.54e - 02$ ($2.40e - 02$)	$6.66e - 02$ ($2.08e - 02$)	$6.29e - 02$ ($2.40e - 02$)
TE[$x \rightarrow y$]	$1.49e - 01$ ($1.59e - 02$)	$1.34e - 01$ ($1.43e - 02$)	$1.26e - 01$ ($1.35e - 02$)	$1.17e - 01$ ($1.23e - 02$)	$1.10e - 01$ ($1.36e - 02$)
CCM[$x \rightarrow y$]	$9.84e - 01$ ($1.46e - 03$)	$9.85e - 01$ ($1.15e - 03$)	$9.86e - 01$ ($1.40e - 03$)	$9.87e - 01$ ($1.33e - 03$)	$9.88e - 01$ ($1.03e - 03$)

Table S5: Clustering results of the neurons in *C. elegans*.

Clusters	Neurons
#1	<u>OLQDL, OLQDR</u> , <u>OLQVL, OLQVR</u> , <u>AIBL, AIBR</u> , AVER, SABVL
#2	RIFR
#3	RIBL, RID, AVBL, RMEV, DB01
#4	<u>RIML, RIMR</u> , <u>AVAL, AVAR</u> , VA01
#5	AVBR, <u>RMEL, RMER</u> , RMED, DB02, VB01, VB02
#6	<u>RIVL, RIVR</u> , <u>SMDVL, SMDVR</u>
#7	SMBDR

* The underlined pairs of neurons are symmetric in position and are clustered in the same cluster.

Table S6: The results for IEE/GC/TE/CCM at their minimum distance OOPs when inferring the *C. elegans* neural connectomes.

	True Positive	True Negative	False Positive	False Negative
IEE	22	15	1	4
GC	22	14	2	4
TE	21	13	3	5
CCM	22	12	4	4

* The true connectomes consist of 7 nodes (42 potential pairs of neurons), with 26 directed causal edges (16 non-causal pairs).

References

1. S. Kato, *et al.*, *Cell* **163**, 656 (2015).
2. S. J. Cook, *et al.*, *Nature* **571**, 63 (2019).
3. A. Banerjee, S. Chandra, E. Ott, *Proceedings of the National Academy of Sciences U.S.A.* **120**, e2216030120 (2023).
4. Emmons Lab, Hermaphrodite and Male Connectomes (Adjacency Matrices), Adults (corrected July 2020), available at <https://wormwiring.org/pages/adjacency.html> (2020). Accessed: 2023-12-15.
5. Ministry of Health, Labour and Welfare, Trend in the number of newly confirmed cases (daily), in Visualizing the data: information on COVID-19 infections, available at <https://covid19.mhlw.go.jp/en/> (2023). Accessed: 2023-10-05.
6. Geospatial Information Authority of Japan, Distances between prefectural offices, in Geographic information of Japan (in Japanese), available at <https://www.gsi.go.jp/KOKUJYOHO/kenchokan.html> (2023). Accessed: 2023-10-12.
7. Ministry of Land, Infrastructure, Transport and Tourism, 2015 Inter-Regional Travel Survey in Japan, in National Trunk Line Passenger Net Flow Survey (in Japanese), available at https://www.mlit.go.jp/sogoseisaku/soukou/sogoseisaku_soukou_fr_000016.html (2019). Accessed: 2023-10-11.
8. Ministry of Land, Infrastructure, Transport and Tourism, 2015 Passenger Regional Flow Survey Dataset, in Portal Site of Official Statistics of Japan (eStat) (in Japanese), available at <https://www.e-stat.go.jp/stat-search/files?tclass=000001056011&cycle=8&year=20151> (2017). Accessed: 2023-10-04.
9. Statistics Bureau of Japan, Population by Sex and Sex Ratio for Prefectures - Total population, Japanese population, October 1, 2021, in Portal Site of Official Statistics of Japan (eStat) (in Japanese), available at <https://www.e-stat.go.jp/stat-search/files?page=1&toukei=00200524&tstat=000000090001> (2022). Accessed: 2024-02-15.
10. S. Leng, *et al.*, *Nature Communications* **11**, 1 (2020).
11. Y. Wang, X.-S. Zhang, L. Chen, *OMICS* **13**, 313 (2009).
12. F. Takens, *Dynamical systems and turbulence, Warwick 1980* (Springer, 1981), pp. 366–381.

13. T. Sauer, J. A. Yorke, M. Casdagli, *Journal of statistical Physics* **65**, 579 (1991).
14. J. Stark, D. Broomhead, M. Davies, J. Huke, *Nonlinear Analysis: Theory, Methods and Applications* **30**, 5303 (1997).
15. B. Cummins, T. Gedeon, K. Spendlove, *SIAM Journal on Applied Dynamical Systems* **14**, 335 (2015).
16. A. Kraskov, H. Stögbauer, P. Grassberger, *Physical Review E* **69**, 066138 (2004).
17. L. Kozachenko, N. N. Leonenko, *Problemy Peredachi Informatsii* **23**, 9 (1987).
18. M. Lindner, R. Vicente, V. Priesemann, M. Wibral, *BMC Neuroscience* **12**, 1 (2011).
19. K. Aihara, T. Takabe, M. Toyoda, *Physics Letters A* **144**, 333 (1990).
20. M. Adachi, K. Aihara, *Neural Networks* **10**, 83 (1997).
21. C. W. J. Granger, *Econometrica* **37**, 424 (1969).
22. T. Schreiber, *Phys. Rev. Lett.* **85**, 461 (2000).
23. G. Sugihara, *et al.*, *Science* **338**, 496 (2012).
24. M. Rota, L. Antolini, M. G. Valsecchi, *BMC Medical Research Methodology* **15**, 24 (2015).
25. J. Shi, L. Chen, K. Aihara, *Journal of the Royal Society Interface* **19**, 20210766 (2022).
26. P. Tao, *et al.*, *Fundamental Research* (2023). In press, available online 6 February 2023.
27. H. Barbosa, *et al.*, *Physics Reports* **734**, 1 (2018).
28. G. K. Zipf, *American Sociological Review* **11**, 677 (1946).
29. S. Kawaguchi, *et al.*, *Biochemical and Biophysical Research Communications* **355**, 555 (2007).
30. R. Morioka, *et al.*, *The Second International Symposium on Optimization and Systems Biology* (2008).
31. H. Ma, K. Aihara, L. Chen, *Scientific Reports* **4**, 7464 (2014).
32. C. H. Ko, J. S. Takahashi, *Human Molecular Genetics* **15**, R271 (2006).
33. H. R. Ueda, *et al.*, *Nature Genetics* **37**, 187 (2005).